The Astrophysical Journal, 574:382–397, 2002 July 20

CHANDRA DISCOVERY OF LUMINOUS SUPERSOFT X-RAY SOURCES IN M81

Douglas A. Swartz,[1] Kajal K. Ghosh,[1] Valery Suleimanov,[2] Allyn F. Tennant,[3] and Kinwah Wu[4]
Received 2001 November 9; accepted 2002 March 28

ABSTRACT

A *Chandra* ACIS-S imaging observation of the nearby galaxy M81 (NGC 3031) reveals nine luminous soft X-ray sources. The local environments, X-ray spectral properties, and X-ray light curves of the sources are presented and discussed in the context of prevailing physical models for supersoft sources. It is shown that the sample falls within expectations based on population synthesis models taken from the literature, although the high observed luminosities ($L_{\rm obs} \sim 2 \times 10^{36}$–$3 \times 10^{38}$ ergs s^{-1} in the 0.2–2.0 keV band) and equivalent blackbody temperatures ($T_{\rm eff} \sim 40$–80 eV) place the brightest detected M81 objects at the high-luminosity end of the class of supersoft sources defined by previous *ROSAT* and *Einstein* studies of nearby galaxies. This is interpreted as a natural consequence of the higher sensitivity of *Chandra* to hotter and more luminous systems. Most of the sources can be explained as canonical supersoft sources: accreting white dwarfs powered by steady surface nuclear burning with X-ray spectra well fitted by hot white dwarf local thermodynamic equilibrium atmosphere models. An exceptionally bright source is scrutinized in greater detail since its estimated bolometric luminosity, $L_{\rm bol} \sim 1.5 \times 10^{39}$ ergs s^{-1}, greatly exceeds theoretical estimates for supersoft sources. This source may be beyond the stability limit and undergoing a phase of mass outflow under extreme conditions. Alternatively, a model in which the observed X-ray spectrum arises from an accretion disk around a black hole of mass $\sim 1200/(\cos i)^{1/2}\ M_{\odot}$ (viewed at an inclination angle i) cannot be excluded.

Subject headings: binaries: symbiotic — stars: atmospheres — stars: evolution — white dwarfs — X-rays: stars

1. INTRODUCTION

Luminous supersoft X-ray sources have effective blackbody temperatures of 15–80 eV and bolometric luminosities of 10^{36}–10^{38} ergs s^{-1} (Kahabka & van den Heuvel 1997).

Lacking significant emission above ~0.5–1 keV, supersoft sources are easily identified using even low-resolution X-ray detectors. However, only 10 Galactic objects are listed as supersoft sources in the latest compilation of Greiner (2000a), while population synthesis studies (Di Stefano & Rappaport 1994; Yungleson et al. 1996; Di Stefano & Nelson 1996) predict that of the order of 1000 supersoft sources could be active in ordinary galaxies like our own. Local objects are therefore of limited use for supersoft source population studies. The best opportunity is to explore nearby galaxies at high Galactic latitude, where intervening absorption is low, all the sources are at a common distance, a single pointing can detect a large number of sources, and their spatial distribution can be measured. Indeed, surveys conducted using the *ROSAT* and *Einstein* observatories have identified eight supersoft sources in the LMC, four in the SMC, and 34 in M31 (see Greiner 1996 for a detailed listing). The high sensitivity and moderate spectral resolution make the *Chandra X-Ray Observatory* an ideal facility to systematically extend supersoft source population studies to other nearby galaxies. This is the rationale for the present investigation.

A 50 ks *Chandra* ACIS-S imaging observation of the nearby galaxy M81 reveals nine supersoft source candidates identified by broadband X-ray colors (§ 2). Four of these sources are located within the old population of bulge stars, and all but one of the remainder are coincident with M81 spiral arms. A search of known objects finds that two of the bulge sources are spatially coincident with sources of enhanced [O III] λ5007 emission, consistent with nebulae photoionized by the X-ray sources. No other spatial correlations were discovered in searches of multiwavelength archival data, contemporary radio and Hα images, or published source catalogs. The two brightest supersoft source candidates are visible in archival *ROSAT* Position Sensitive Proportional Counter (PSPC) or HRI X-ray images.

Detailed X-ray spectral analysis of the three brightest sources is presented in § 3. Their effective temperatures, based on line-blanketed local thermodynamic equilibrium white dwarf atmospheres and blackbody model fits, span $T_{\rm eff} \sim 50$–80 eV. The corresponding inferred bolometric luminosities are $L_{\rm bol} \sim 3 \times 10^{38}$–$1.5 \times 10^{39}$ ergs s^{-1}, ranking the brightest M81 objects among the hottest and brightest of all previously known supersoft sources. Extrapolating the spectral fits to the fainter sources implies that the observed luminosities of the M81 supersoft source population range from $L_{\rm obs} \sim 2 \times 10^{36}$ (near the sensitivity limit) to $\sim 3 \times 10^{38}$ ergs s^{-1} in the 0.2–2.0 keV band. The brightest sources show signs of X-ray variability over the duration of the *Chandra* observation and over the approximately 10 yr light curve observed by *ROSAT* (§ 4).

The X-ray signatures of the M81 sources are compared to well-studied objects in the (rather heterogeneous) class of supersoft sources in an effort to identify possible physical mechanisms responsible for the observed emission (§ 5). The brightest source cannot easily be explained by prevailing theory, while the other two sources for which reliable spectral fits can be made show strong similarities to the hot close

[1] Universities Space Research Association, NASA Marshall Space Flight Center, SD50, Huntsville, AL 35812.
[2] Kazan State University, Kremlevskaya str. 18, 420008 Kazan, Russia.
[3] Space Science Department, NASA Marshall Space Flight Center, SD50, Huntsville, AL 35812.
[4] MSSL, University College London, Holmbury St. Mary, Surrey, RH5 6NT, UK; and School of Physics, University of Sydney, NSW 2006, Australia.

binary accreting white dwarf (WD) systems CAL 87 and CAL 83. Some prospects for future observations are discussed (§ 6), and a comparison is made to the supersoft source populations observed in M31 with *ROSAT* (Supper et al. 1997; Kahabka 1999) and in M101 with *Chandra* (Pence et al. 2001).

2. OBSERVATION OF SUPERSOFT SOURCES IN M81

A 49,926 s observation of a portion of the galaxy M81 was obtained with the *Chandra* Advanced CCD Imaging Spectrometer (ACIS) on 2000 May 7. The nucleus and bulge of the galaxy were located near the center of the back-illuminated S3 device of the spectroscopy array operating in imaging mode. The observation was taken in faint timed exposure mode at 3.241 s frame^{-1}. The global properties of the sources detected in this data are given in Tennant et al. (2001). Standard *Chandra* X-Ray Center processing has applied aspect corrections and compensated for spacecraft dither. A charge transfer inefficiency (CTI) corrector algorithm (Townsley et al. 2000)[5] was then applied to the level 1 event list to partially correct for the charge loss and charge-smearing effects of CTI in the ACIS detectors. The data were then cleaned of bad pixels and columns. We selected the standard-grade set and events in pulse invariant (PI) channels corresponding to ~0.1–8.0 keV for source detection (§ 2.1) and ~0.2–2.0 keV for spectral analysis (§ 3). The 50 ks exposure corresponds to a limiting supersoft source observed 0.2–2.0 keV luminosity of $\sim 2 \times 10^{36}$ ergs s^{-1} for a 3 σ signal-to-noise ratio, assuming that the weak supersoft source candidates have the same spectrum as the brightest object in the class.

The detector viewing area covers 57% of the optical extent of the galaxy, defined as the ellipse of major diameter 26.′9, corresponding to the D_{25} diameter (the major diameter of the $m_B = 25$ mag arcsec^{-1} iosphote) as tabulated in de Vaucouleurs et al. (1991), oriented at position angle 157° and with major-to-minor axis ratio 2 : 1 corresponding to the 60° inclination angle of M81. This area includes all of the back-illuminated (BI) S3 device, approximately half of each of the front-illuminated (FI) S2 and S4 devices, and the outer corner of the FI device I3. The data from each device are analyzed independently because of differing energy resolutions, low-energy responses, and background signals.

In addition to this primary data set, a 2.4 ks ACIS-S image taken on 2000 March 21 and numerous *ROSAT* PSPC and HRI data sets were used to construct long-term light curves of the brightest sources (see Immler & Wang 2001 for details of the *ROSAT* observations).

2.1. *Source Identification Criteria*

X-ray sources were identified using the source detection method described in Tennant et al. (2001) that compares the data to an analytic function that approximately matches the telescope's point-spread function (PSF) and includes off-axis broadening. Small spatial regions centered on each source with a size encompassing the 95% encircled energy radii of the PSF (at 1.5 keV) were then selected for analysis. These regions are less than 2″ in diameter on-axis and exceed 10″ only for sources $\gtrsim 8'$ off-axis.

[5] Matching response matrices were also provided by L. Townsley.

Background-subtracted source counts were binned into three broad bands defined as S (0.3–1.0 keV), M (1.0–2.0 keV), and H (2.0–8.0 keV), and the X-ray colors $MS \equiv (M - S)/(M + S)$ and $HS \equiv (H - S)/(H + S)$ were constructed. For this purpose, two background spectra were defined for sources on S3: one for the bulge where contributions from the wings of the PSF of the bright nucleus and from a relatively high level of unresolved X-ray emission were previously detected in the data (Tennant et al. 2001) and another for the disk. Separate background spectra are defined for sources on S2 and S4. In all cases, regions enclosing all identified sources are first excluded from the data and then the spectrum of the remaining area was assigned to the background. Figure 1 shows the resulting background-corrected color-color diagram for all 81 sources detected on S3 above a signal-to-noise ratio of 3.5 (Tennant et al. 2001). The bulge and disk background spectra are also represented. Some faint sources far from the aim point are background-dominated. Their background-subtracted count rates in certain energy bands can be negative, and the absolute values of their resulting colors may exceed unity, as seen in Figure 1.

Supersoft sources lie near $(-1, -1)$ in this figure (no emission above 1.0 keV). Those sources with color values ($MS < -0.5$, $HS < -0.5$) were tentatively classified as supersoft sources. This criterion selects 10 sources on S3, two sources on S2, and none on the remaining CCDs.

The list of sources was compared to catalogs of objects to eliminate those with properties inconsistent with supersoft sources. Supernova remnant candidate 17 in the catalog of Matonick & Fesen (1997) lies within the positional uncertainty of one of the supersoft source candidates detected on S3. Although this source is weak, its spectrum appears more similar to the other X-ray sources associated with super-

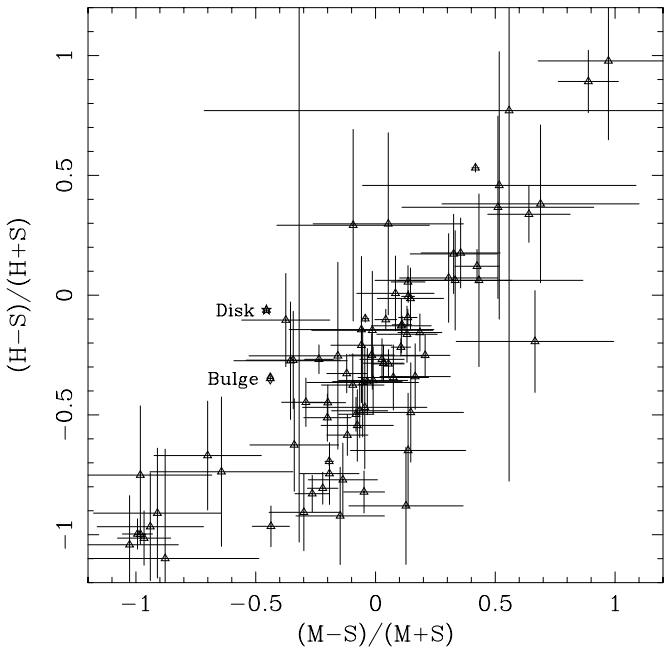

FIG. 1.—X-ray color-color diagram for M81 sources on the BI device S3. Background-subtracted source counts are binned into three bands: S (0.3–1.0 keV), M (1.0–2.0 keV), and H (2.0–8.0 keV). Points labeled "Disk" and "Bulge" represent the colors of the background spectra in these two regions.

nova remnants than to the other supersoft source candidates. Matonick & Fesen (1997) report an [O III]/Hα ratio for the supernova remnant candidate of 0.6 and an [S II]/Hα ratio of 1.2. Rappaport, Di Stefano, & Smith (1994b) predict far different ratios, 2.4–6.1 and 0.1–0.5, for ionized regions surrounding supersoft sources. This source is therefore excluded from the list of candidate supersoft sources even though its colors ($MS = -0.88 \pm 0.39$, $HS = -1.10 \pm 0.45$) lie within our selection criteria.

Both candidate sources on S2 are coincident with bright ($m_V \sim 9$ mag) G0 stars in the Positions and Proper Motions catalog of stars. While they have X-ray colors (MS, HS) $\sim$ (-0.6, -0.8), they are excluded from further consideration.

The positions of the remaining candidate supersoft sources were compared to optical features in Digitized Sky Survey (DSS) and archival *Hubble Space Telescope* (*HST*) WFPC2 images to search for potential uncataloged foreground objects. Late-type stars with active coronae and AM Her–type magnetic cataclysmic variables (CVs) are the only foreground objects with X-ray colors falling within our selection criteria. Foreground late-type stars are easily identified in optical images since their X-ray flux is typically a small fraction of their optical flux. Am Her–type magnetic CVs have a soft component ($T \sim$ 10–100 eV) that may dominate any hard bremsstrahlung ($kT \sim 10$ keV) component and appear supersoft. However, their K or M star companions should be visible optically out to distances well beyond the Galactic disk in the direction of M81. It remains possible that some of the weakest supersoft source candidates could be very bright CVs, with late M-type companions, and escape optical detection provided that they are located some $\sim$7 kpc above the plane of the Galaxy.

The observed properties of the remaining nine candidate supersoft sources, all located on the BI S3 device, are listed in Table 1, and their positions are shown superimposed on the second-generation DSS image of M81 in Figure 2. Hereafter, individual supersoft sources in M81 will be referred to in order of observed brightness, column (1) of Table 1, as source N1 through source N9.

The lack of candidate supersoft sources on the FI devices is attributable to the small fraction of M81 falling within the viewing field of the FI devices, to the scarcity of X-ray sources (of all types) found far from the central regions of M81, to the weaker low-energy response of the FI devices, and to the decreased off-axis source sensitivity. The detection limit for supersoft sources on the FI devices is $\sim 1.2 \times 10^{37}$ ergs s^{-1} or about 6 times brighter than the corresponding limit on the BI device S3.

TABLE 1
OBSERVED SUPERSOFT SOURCES IN M81

Source Number (1)	R.A. (2000.0) (2)	Decl. (2000.0) (3)	Flux[a] (4)	Location (5)
1	09 55 42.15	69 03 36.2	74.95	Bulge
2	09 56 08.96	69 01 06.6	10.24	Arm
3	09 55 53.00	69 05 20.3	3.30	Arm
4	09 55 28.38	69 02 44.6	1.09	Bulge
5	09 55 37.58	69 03 16.2	0.95	Bulge
6	09 55 55.97	69 03 12.5	0.78	Bulge
7	09 56 14.16	69 02 26.2	0.63	Disk
8	09 55 47.92	68 59 28.2	0.59	Arm
9	09 55 48.13	68 59 15.5	0.41	Arm

NOTE.—Units of right ascension are hours, minutes, and seconds, and units of declination are degrees, arcminutes, and arcseconds.

[a] Background-subtracted, 0.2–2.0 keV, in units of 10^{-3} counts s^{-1}.

2.2. *Local Source Environments*

None of the candidate supersoft sources appear extended in the *Chandra* data. As listed in Table 1, candidate sources are found throughout the bulge and disk of M81, and several lie within $\sim$200 pc of spiral arms ($1' = 1.086$ kpc for the adopted distance of 3.6 Mpc to M81; Freedman et al. 1994).

While several of the candidate supersoft sources are in crowded, source-rich regions of this well-studied galaxy, only two can be unequivocally identified with cataloged objects observed at other wavelengths based on positional coincidence. These are the bulge sources N4 and N5. Three of the four bulge supersoft source candidates lie within the $\sim 4'$ observing field of the [O III] λ5007 survey of M81 planetary nebulae (PNs) performed by Jacoby et al. (1989). Source N4 is coincident with object ID 68 (apparent magnitude 25.33 at 5007 Å), and source N5 is coincident with object ID 116 (apparent magnitude 24.78) in the list of Jacoby et al. (1989). The observed X-ray luminosities of these sources exceed those of PNs (10^{30}–10^{32} ergs s^{-1}) by several orders of magnitude, assuming they are at the distance of M81. The one known exception is 1E 0056.8$-$7154, a supersoft source associated with the Small Magellanic Cloud PN N67 (Wang 1991) with a bolometric luminosity of 2×10^{37} ergs s^{-1} (Heise, van Teeseling, & Kahabka 1994). The lack of detectable emission at other wavelengths, particularly in *HST* WFPC2 images, indicates that they are not foreground objects lying, by chance, along the line of sight. Instead, the [O III] λ5007 emission could come from regions ionized by the X-ray source in a way similar to that observed in the LMC supersoft source CAL 83 (Remillard, Rappaport, & Macri 1995). The flux observed by Jacoby et al. (1989) is consistent with the supersoft source ionization model predictions of Rappaport et al. (1994a). This is discussed in more detail in § 5.2.4.

There are no pointlike objects observed at other wavelengths spatially coincident with any of the remaining supersoft source candidates in M81. It is noteworthy that the exceptionally X-ray bright source N1 is within the field observed by Jacoby et al. (1989) and the recent survey of Magini et al. (2001) but is not seen at [O III] λ5007. This source lies in a featureless region of the bulge dominated in optical bands by a high density of unresolved bulge stars. There is no nearby object discernible in archival *HST* WFPC2 images of the region nor in UV images centered at 2490 and 1520 Å (Hill et al. 1992), a recent (2001 May 21; A. Shafter 2001, private communication) CCD image taken through a 70 Å wide Hα filter, the continuum-subtracted Hα data of Devereux, Jacoby, & Ciardullo (1995), the 6 and 20 cm radio continuum observations reported by Kaufman et al. (1996), or recent 6 cm data (T. Pannuti 2001, private communication).

3. X-RAY SPECTRAL ANALYSIS

The spectra of all nine candidate sources are shown in Figure 3. They typically show a rise from low energies to a peak at $\sim$0.45–0.7 keV followed by a rapid decline toward

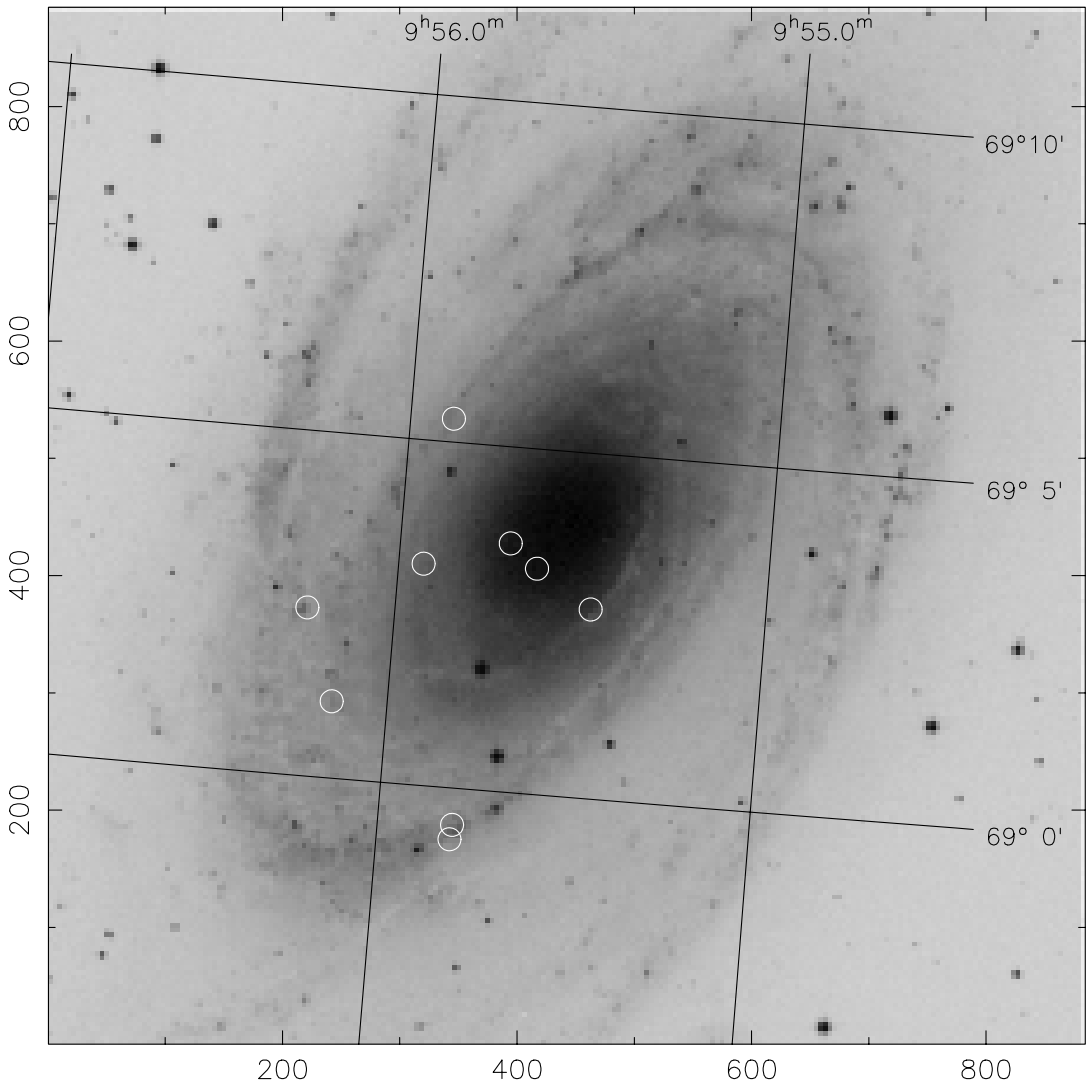

FIG. 2.—Digitized Sky Survey image of M81 with the positions of the nine X-ray–detected supersoft source candidates superposed. Image is $\sim 15' \times 15'$. Circles have $10''$ radii.

higher energies. The shape of the low-energy portion of the spectra is determined by a combination of extinction and a decreasing ACIS detection efficiency at low energies. Above the peak, the shape is determined by a roughly exponential decline of the intrinsic source spectra.

In spectra such as these, the inferred bolometric luminosity is much higher than that observed with the peak of the intrinsic spectral energy distribution occurring at energies lower than observed. The inferred luminosities are very sensitive to the model parameters and to calibration uncertainties in the low-energy response of the BI devices. Although there is often significant flux below 0.2 keV, data at energies below this value were excluded from the fitting because of these uncertainties.

A sufficient number of counts for spectral analysis were accumulated from only the three brightest sources listed in Table 1. The spatial regions selected for spectral analysis were chosen to be centered on each source as described above (§ 2.1). Accompanying background spectra were extracted for each source from annular regions centered on the source with inner and outer radii of 30 and 50 pixels, respectively, and containing of order of 200 counts. Note that this procedure differs from the large background regions selected for constructing the broadband colors described previously. The procedure used in this section more accurately represents local variations in background. Spectra have been grouped into spectral bins containing a minimum of 20 counts and fitted using the XSPEC spectral fitting package (Arnaud 1996) to blackbody and model atmosphere spectra of hot white dwarfs calculated in the local thermodynamic equilibrium (LTE) approximation.

The X-ray emission from supersoft sources is believed to originate from nuclear burning on the surface of a WD star. The nuclear burning takes place at high optical depth within a geometrically thin, high-density atmosphere, with the resulting emergent spectrum highly modified by the cooler outer layers. Under these conditions, hot WD LTE model atmosphere spectra are a more appropriate approximation than is a simple blackbody assumption. Therefore, we developed tables of plane-parallel LTE model atmospheres as an alternative model for spectral fitting. Under certain circumstances the WD atmosphere may become extended or even

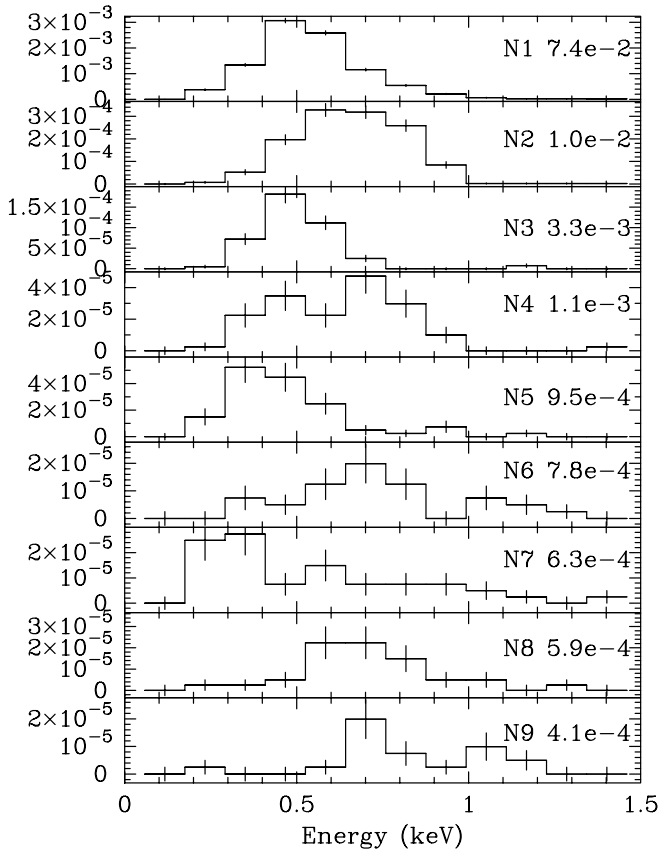

FIG. 3.—Spectra of nine supersoft source candidates. Labels denote source number and count rates over the 0.2–2.0 keV *Chandra* energy band (Table 1). Data have been binned by eight PI channels (~117 eV). Vertical axis units are counts per second.

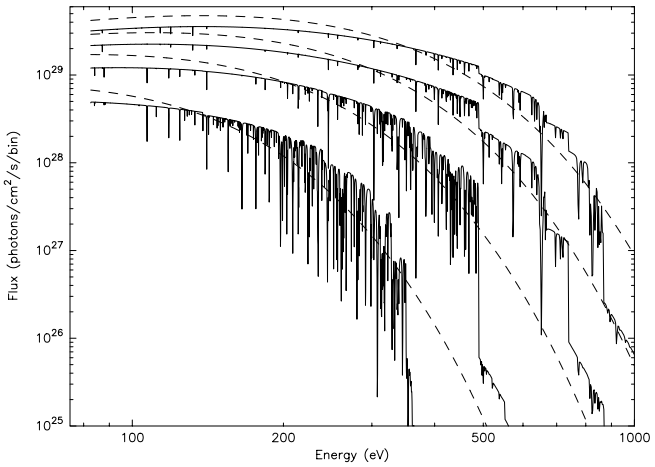

FIG. 4.—Hot white dwarf LTE atmosphere model spectra (*solid line*) and corresponding blackbody spectra (*dashed line*) at four effective temperatures and a solar abundance composition. From top to bottom, the temperatures are $T_{\rm eff}/10^5$ K = 10, 8, 6, and 4. The surface gravity is $\log g = 9$ except for the hottest model where $\log g = 9.5$ to avoid exceeding the Eddington limit luminosity. Prominent bound-free edges are apparent at 490 (C VI), 670 (N VII), 740 (O VII), and 870 eV (O VIII).

partially ejected as a result of rapid nuclear burning. Spectra of extended, expanding, spherical atmospheres tend to be flatter than that from plane-parallel hydrostatic atmospheres with the same color temperature at maximum flux. Model atmospheres including an optically thick wind are currently in preparation.

The fundamental parameters of our plane-parallel LTE model atmospheres are the effective temperature $T_{\rm eff}$, surface gravity g, and luminosity scale factor $K = L/(4\pi\sigma T_{\rm eff}^4 D^2)$, where L is the bolometric luminosity, σ is the Stefan-Boltzmann constant, and D is the distance from the source to the observer. The model atmospheres were constructed following standard temperature correction procedures as outlined in Mihalas (1978) in order to satisfy the hydrostatic and radiative equilibrium constraints. The 15 most abundant elements from H through Ni are included with bound-free opacities computed from the photoionization cross sections of Verner et al. (1993) and Verner & Yakovlev (1995). Line blanketing is included using ~1200 of the strongest spectral lines from the CHIANTI, Version 3.0, atomic database (Dere et al. 1997).

A series of LTE model atmosphere spectra were constructed in this fashion spanning the range of parameters 10^5 K $\leq T_{\rm eff} \leq 1.3 \times 10^6$ K and $7.5 \leq \log g \leq 9.5$, as appropriate for WD atmospheres, with the scale factor K used as the model normalization in XSPEC. Tables of these models were used in conjunction with a photoelectric absorption component in fitting to the observed spectra. A separate table was constructed for each of two values of photospheric metal abundances, $Z/Z_\odot = 1$ and $Z/Z_\odot = 0.01$, relative to the solar composition given by Anders & Grevesse (1989). The lower metal abundance is roughly compatible with the observed M81 metallicities (~0.03) recently reported by Kong et al. (2000). In addition, an He-rich model consisting of $Z/Z_\odot = 0.03$ metals and 99% He by weight was also constructed.

For reference, computed hot WD LTE model atmosphere spectra at several temperatures are shown in Figure 4. Many of the edges seen in these spectra will prove to be key diagnostics of the properties of the candidate supersoft sources.

3.1. *Source N1*

The spectral fit results for the brightest supersoft source candidate, source N1, are listed in Table 2. This and subsequent tables for the other bright sources include one column for each model. Rows list the χ^2 fit statistic, the fitted model parameters $N_{\rm H}$ (hydrogen column density), $T_{\rm eff}$ (blackbody or effective temperature), $\log g$ (surface gravity), $E_{\rm edge}$ (absorption edge energy), and the accompanying τ (edge optical depth). All models include photoelectric absorption from a solar abundance column. In the case of the model "zvarabs," the abundance of C and O in the absorbing column is allowed to vary. The table lists the enhancement of these elements relative to the solar values. Also listed are the observed luminosity $L_{\rm obs}$ in the 0.2–2.0 keV band, the unabsorbed luminosity $L_{\rm X}$ in the same band, and the bolometric luminosity $L_{\rm bol}$, as scaled from the model normalizations assuming a distance of 3.6 Mpc to M81.

The observed spectrum, best-fit absorbed blackbody model with added absorption edge at 0.26 keV (second model of Table 2), and fit residuals for source N1 are shown in Figure 5. A simple blackbody model is statistically superior to either of the LTE WD atmosphere models because of the lack of absorption edges in the observed spectrum. However, there is a feature in the blackbody fit residuals near 0.3 keV. This feature can be modeled as an edge at 0.26 ± 0.01 keV (second column of Table 2), which is very

TABLE 2
MODEL FITS FOR SOURCE N1

Model[a]	Blackbody	Blackbody + Edge	Blackbody with zvarabs[b]	LTE $Z = Z_\odot$	LTE $Z = 0.01\,Z_\odot$	LTE + Ray $Z = Z_\odot$	diskbb
χ^2_ν / dof	1.40 / 47	0.98 / 45	1.05 / 44	2.75 / 46	3.55 / 47	1.24 / 44	1.61 / 47
N_H / 10^{20} cm^{-2}	$5.7^{+0.7}_{-0.6}$	$4.2^{+1.0}_{-1.3}$	$6.3^{+0.5}_{-0.5}$	$4.2^{+0.6}_{-0.4}$	$4.0^{+0.6}_{-0.4}$	$4.4^{+0.5}_{-0.6}$	$7.4^{+0.8}_{-0.8}$
$T_{\rm eff}$ (eV)	86^{+2}_{-3}	81^{+3}_{-4}	78^{+3}_{-3}	69^{+1}_{-1}	64^{+2}_{-1}	66^{+1}_{-1}	100^{+4}_{-3}
$E_{\rm edge}$ (keV), τ	...	$0.26^{+0.02}_{-0.02}$, 1.6	...	...	...	...	...
C, O enhancement	...	...	$6.6^{+1.7}_{-1.7}$, $1.5^{0.9}_{2.1}$	...	...	...	...
log g (cm^2 s^{-1})	...	...	...	$8.7^{+0.04}_{-0.04}$	$8.8^{+0.05}_{-0.03}$	$8.5^{+0.03}_{-0.1}$	...
Thermal $kT, f(L_X)$[c]	...	...	...	...	...	$0.35^{+0.12}_{0.07}$, 0.18	...
$L_{\rm obs}$ / 10^{38} ergs s^{-1}	$3.0^{+0.02}_{-0.02}$	$3.0^{+0.04}_{-0.04}$	$2.9^{+0.02}_{-0.03}$	$2.9^{+0.02}_{-0.02}$	$2.9^{+0.04}_{-0.04}$	$3.0^{+0.01}_{-0.01}$	$3.0^{+0.03}_{-0.03}$
L_X / 10^{38} ergs s^{-1}	$8.7^{+1.6}_{-1.2}$	$7.3^{+2.9}_{-1.7}$	$8.8^{+1.4}_{-4.7}$	$6.3^{+1.4}_{-1.4}$	$6.2^{+1.6}_{-1.5}$	$6.7^{+0.6}_{-0.6}$	$13.4^{+3.0}_{-2.9}$
$L_{\rm bol}$ / 10^{38} ergs s^{-1}	$12.0^{+2.0}_{-2.1}$	$15.0^{+5.2}_{-1.1}$	$23.0^{+11.2}_{-8.0}$	$9.0^{+2.0}_{-1.1}$	$8.0^{+1.3}_{-1.1}$	$9.0^{+2.4}_{-2.1}$	$11.0^{+1.4}_{-1.0}$ / cos$i$

[a] All models include solar abundance absorption column.
[b] Variable abundance absorption column with best-fit redshift $z = 0.04$.
[c] Raymond-Smith model temperature (in units of keV) and fraction of L_X due to this component.

close to the neutral C K edge at 0.277 keV. Since there is no reason to expect the Galactic absorbing column to have exactly solar abundances, we also tried a variable abundance model. If a small "redshift" ($z = 0.04$) is applied, this model also provided an excellent fit to the data, as shown by the third column in Table 2. It is worth noting that the ACIS energy scale is uncertain at the lowest energies, and thus the feature is likely a carbon edge, and the redshift is due to this uncertainty. Since the ACIS response is also uncertain at these energies, we cannot determine whether the excess carbon is intrinsic to the source in M81, lies within our Galaxy, or is a detector effect.

LTE models with an additional Raymond-Smith thermal emission component are an improvement over the single LTE component models because this added thermal component tends to fill the ~0.7–1.0 keV region of the model spectrum underestimated because of the presence of absorption edges in the LTE component. While the physical basis for such a thermal component has precedence in modeling of, e.g., the recurrent nova U Sco (Kahabka, Parmar, & Hartmann 1999b) and the symbiotic nova SMC 3 (Jordan et al. 1996) and there is reason to believe source N1 may be near a state of dynamical outflow (see discussion in § 5), the fact that a simple blackbody model provides an equally acceptable fit allows one to conclude that the thermal component is not necessary. It should be noted that ~2% of the incident flux at 0.5 keV is piled up in the spectrum of source N1, resulting in detected events near 1 keV. The observed flux at 1.0–1.1 keV is 3.5% of that in the 0.5–0.55 keV band. Thus, some 60% of the observed flux at 1.0–1.1 keV is due to pileup.

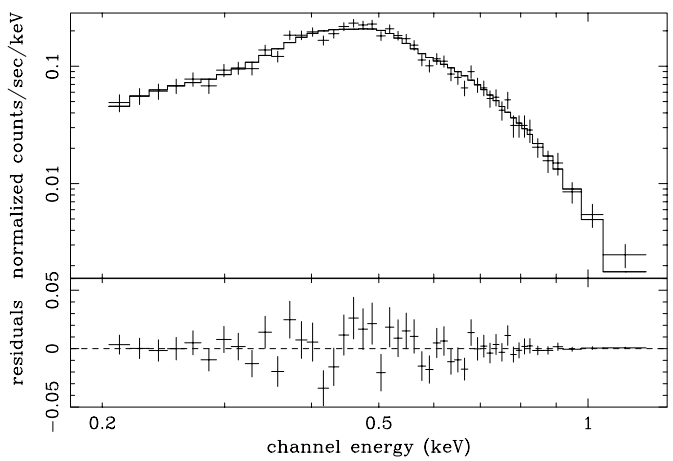

FIG. 5.—*Top*: Observed spectrum of source N1 (*symbols*) and best-fit blackbody model with solar abundance photoelectric absorption and added absorption edge at 0.26 keV (*solid line*). *Bottom*: Fit residuals.

He-rich LTE model atmospheres were also fitted to this spectrum, but no statistically acceptable fits were obtained, and they are omitted from Table 2 for brevity. The larger He opacity near the He II edge in these models leads to a slightly lower temperature and a slightly steeper temperature gradient in spectrum-forming ($0.1 \lesssim \tau_R \lesssim 1$, where τ_R is the Rosseland mean opacity) regions of the atmosphere. The emergent flux therefore decreases near the He II edge (because of lower temperatures) and increases slightly at the peak of the spectral energy distribution (because of the steeper gradient). The overall effect in the *Chandra* observable energy band is to produce a steeper spectrum than the H-rich LTE models. The spectrum is further steepened by the bound-free edges from intermediate-mass metals resulting in a poorer model of the data.

The blackbody shape of the observed spectrum of source N1 is reminiscent of that expected from a geometrically thin, optically thick accretion disk surrounding a black hole (Shakura & Sunyaev 1973). For completeness, therefore, an accretion disk emission model was also fitted to the observations. This model accumulates the spectrum from an optically thick accretion disk observed at inclination angle i from a superposition of blackbody spectra from concentric annular elements representing the radial dependence of the disk temperature profile (Mitsuda et al. 1984; Makishima et al. 1986). The model parameters (model "diskbb," Table 2) are the normalization, proportional to the innermost disk radius $R_{\rm in}$, for a known inclination angle and distance to the source and the temperature at $R_{\rm in}$. Assuming that $R_{\rm in}$ corresponds to the last stable Keplerian orbit (Makishima et al. 2000) implies a mass for the central object. The best-fit normalization for source N1 corresponds to a black hole mass $M_{\rm BH} \sim 1200/(\cos i)^{-1/2}$ assuming that the last stable orbit is at three Schwarzschild radii. The best-fit temperature at $R_{\rm in}$, $T_{\rm in} \sim 100$ eV, implies a bolometric luminosity $L_{\rm bol} \sim 10^{39}$ ergs s^{-1}. Not surprisingly, the color temperature

$T_{\rm in}$ is slightly higher than that obtained from the blackbody models. The shape of the blackbody disk model is a power law of photon index $-\frac{2}{3}$ at low photon energies steepening to the Wien portion of a blackbody of temperature $T_{\rm bb} = 0.7T_{\rm in}$ at higher energies (Makishima et al. 1986). Thus, the combination of an innermost disk radius temperature slightly higher than the blackbody model temperature and a higher absorption column density is just what is needed to make the disk blackbody model mimic a standard blackbody spectrum. This is especially true in view of the fact that only the steep Wien portion of the spectrum lies within the *Chandra* energy band for low values of $T_{\rm in}$ and the power-law portion of the blackbody disk model spectrum lies entirely below the low-energy instrumental cutoff. The lack of detectable emission at longer wavelengths at the position of source N1 (§ 2.2) and the lack of an observable hard power-law tail argues against the blackbody disk model.

The luminosity of source N1 is exceptionally high. The observed 0.2–2.0 keV luminosity, $L_{\rm obs} \sim 3 \times 10^{38}$ ergs s^{-1}, is slightly above the Eddington limit for a 1.4 $M_\odot$ H-accreting star. The unabsorbed luminosity on the same energy range and the inferred bolometric luminosities are much higher, although with high uncertainties. In contrast, $L_{\rm obs}$ is tightly constrained and its value does not vary among the models (Table 2). Another source of uncertainty, independent of model fit uncertainties, is the gain behavior in the BI device at low photon energies and at the -120°C focal plane temperature in use at the time of observation. Very nearly $\frac{1}{3}$ of the observed flux from source N1 falls in the 0.2–0.4 keV energy band. A 20% uncertainty in the flux below 0.4 keV corresponds, therefore, to an additional 7% uncertainty in $L_{\rm obs}$. Conservatively, then, the estimated bolometric luminosity of source N1 is at least several times 10^{38} ergs s^{-1} and, depending on the model, may be as high as a few 10^{39} ergs s^{-1}. This result places severe constraints on physical models for this source (§ 5).

It is notable that the large range of $L_{\rm X}$ and $L_{\rm bol}$ values is not obviously reflected in a large range of the model fit parameters $N_{\rm H}$ and $T_{\rm eff}$. From Table 2, the ranges of these parameters among the various models (excluding diskbb) are $N_{\rm H} = (4.9 \pm 2.0) \times 10^{20}$ cm^{-2} and $T_{\rm eff} = 75 \pm 11$ eV. This substantiates the previous conjecture that the inferred luminosities are very sensitive to small variations in the model parameters. However, the differences in shape of the blackbody and LTE model atmosphere spectra do not give systematically large differences in the derived temperatures, column densities, and luminosities, as is often reported for supersoft sources.

The hot WD LTE model parameter $\log g$ is directly related to the mass of the assumed white dwarf. The resulting white dwarf mass is estimated to be 0.9–1.1 $M_\odot$ for source N1.

3.2. *Source N2*

The spectral fit results for source N2 are listed in Table 3. The observed spectrum, best-fit LTE atmosphere model, and fit residuals are shown in Figure 6.

In contrast to source N1, a blackbody model is clearly a poor fit to the data. A blackbody with an added absorption edge at $0.85^{+0.01}_{-0.03}$ keV gives a better fit, suggesting the presence of highly ionized O in a very hot atmosphere. The LTE models provide significant improvements over the blackbody model. The results are not very sensitive to the assumed metal abundances, although the 1% solar metal abundance model provides an improved fit. At the derived temperatures, $T_{\rm eff} \sim 67$–69 eV, the hot WD LTE models produce numerous absorption edges. When convolved with the instrument response, the most prominent edges are those from highly ionized O at 740 (O VII) and 870 eV (O VIII). In the low-abundance model, the edges are not as deep, and an additional Ne IX edge (1196 eV) appears in the model but is statistically insignificant in the fit.

TABLE 3
MODEL FITS FOR SOURCE N2

Blackbody Model Fits		
Model[a]	Blackbody	Blackbody with Edge
χ^2_ν / dof	1.87 / 16	0.93 / 14
$N_{\rm H}$ / 10^{20} cm^{-2}	$19.8^{+8.0}_{-7.5}$	$9.3^{+5.2}_{-5.7}$
$T_{\rm eff}$(eV)	98^{+15}_{-11}	171^{+60}_{-29}
$E_{\rm edge}$(keV), τ	...	$0.85^{+0.01}_{-0.03}$, 3.8
$L_{\rm obs}$ / 10^{38} ergs s^{-1}	$0.4^{+0.02}_{-0.02}$	$0.5^{+0.04}_{-0.04}$
$L_{\rm X}$ / 10^{38} ergs s^{-1}	$3.2^{+5.9}_{-2.1}$	$0.9^{+1.4}_{-0.3}$
$L_{\rm bol}$ / 10^{38} ergs s^{-1}	$4.0^{+4.9}_{-0.5}$	$1.3^{+0.7}_{-0.3}$
LTE Atmosphere Model Fits		
Model[a]	$Z = Z_\odot$	$Z = 0.01\,Z_\odot$
χ^2_ν / dof	1.38 / 15	1.00 / 15
$N_{\rm H}$ / 10^{20} cm^{-2}	$25.0^{+7.1}_{-8.4}$	$15.8^{+3.8}_{-4.2}$
$T_{\rm eff}$ (eV)	69^{+4}_{-1}	67^{+2}_{-1}
$\log g$ cm^2 s^{-1}	$8.49^{+0.03}_{-0.03}$	$8.24^{+0.40}_{-0.08}$
$L_{\rm obs}$ / 10^{38} ergs s^{-1}	$0.3^{+0.01}_{-0.01}$	$0.4^{+0.03}_{-0.03}$
$L_{\rm X}$ / 10^{38} ergs s^{-1}	$4.5^{+1.4}_{-3.7}$	$2.0^{+1.5}_{-0.8}$
$L_{\rm bol}$ / 10^{38} ergs s^{-1}	$6.4^{+3.9}_{-1.3}$	$5.3^{+4.8}_{-2.1}$

[a] All models include solar abundance absorption column.

The observed 0.2–2.0 keV luminosity derived from the hot WD LTE model atmosphere spectrum is much less than the Eddington limit for a hydrogen-accreting WD. The inferred range of bolometric luminosities exceeds this limit by a factor of 2–3. The white dwarf mass inferred from the LTE models is 0.7–0.9 $M_\odot$.

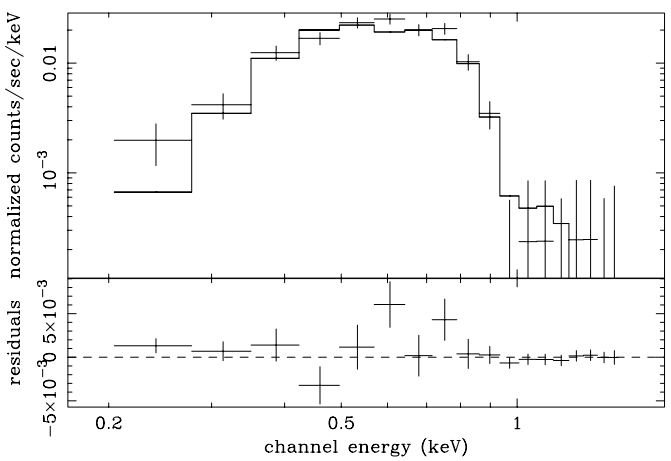

FIG. 6.—*Top*: Observed spectrum of source N2 (*symbols*), best-fit LTE WD model atmosphere spectrum with 1% solar abundance metals, and solar abundance photoelectric absorption (*solid line*). *Bottom*: Fit residuals.

TABLE 4
MODEL FITS FOR SOURCE N3

Model[a]	Blackbody	$Z = Z_\odot$	$Z = 0.01\,Z_\odot$
χ^2_ν / dof	0.94 / 4	0.90 / 3	1.4 / 3
N_H / 10^{20} cm^{-2}	$10.7^{+12.6}_{-7.1}$	$4.7^{+5.3}_{-3.2}$	$8.7^{+5.4}_{-4.3}$
T_{eff} (eV)	52^{+13}_{-5}	52^{+1}_{-1}	45^{+9}_{-6}
log g (cm^2 s^{-1})	...	$7.9^{+0.9}_{-0.1}$	$9.2^{+0.2}_{-1.6}$
L_{obs} / 10^{38} ergs s^{-1}	$0.1^{+0.03}_{-0.03}$	$0.1^{+0.02}_{-0.02}$	$0.1^{+0.03}_{-0.02}$
L_X / 10^{38} ergs s^{-1}	$2.0^{+4.5}_{-1.3}$	$0.4^{+0.3}_{-0.2}$	$1.0^{+1.9}_{-0.9}$
L_{bol} / 10^{38} ergs s^{-1}	$4.6^{+15.3}_{-3.4}$	$1.2^{+1.3}_{-0.7}$	$1.8^{+8.0}_{-1.2}$

[a] All models include solar abundance absorption column.

3.3. *Source N3*

The spectral fit results for source N3 are listed in Table 4. The observed spectrum, best-fit hot WD LTE model atmosphere spectrum, and fit residuals are shown in Figure 7.

Unlike the stronger sources, the spectrum of source N3 is fitted equally well by all three models, and there is no spectral feature to meaningfully discriminate between models. In particular, the lack of flux above ~0.7 keV means that the dominant absorption edges present in the LTE atmosphere models are the relatively weak edges at C VI (490 eV) and N VII (670 eV). In this case, a slightly more absorbed blackbody model relative to the LTE models adequately mimics the observed steep decline above ~0.5 keV.

The observed 0.2–2.0 keV luminosity L_{obs} is less than the Eddington limit for a hydrogen-accreting WD, and L_{bol} is comparable to the Eddington limit, although again, it is highly uncertain. The white dwarf mass inferred from the WD atmosphere LTE models is ~0.5 $M_\odot$ for the solar abundance model and is effectively unconstrained by the 1% solar metallicity model.

3.4. *Other Sources*

Statistically constrained model fits to the remaining sources could not be achieved. The observed count rates and similarities to the spectra of the brighter sources allow a crude extrapolation of the derived luminosities of the brighter sources to the remaining sources by the following reasoning: the ratio $L_{bol}/L_{obs} \sim 5$ for source N1 and ~10–20 for sources N2 and N3. The latter two sources are associated with spiral arms. They have higher absorbing columns than source N1, which accounts for the higher L_{bol}/L_{obs} ratio. An estimate of L_{bol} can be made by assuming that the ratio $L_{bol}/L_{obs} = 15$ for sources on the spiral arms and equals 5 otherwise and noting that L_{obs} is proportional to the observed count rate (Table 1). Applying this approximation to the remaining sources using the data from Table 1 gives the following values of L_{bol} in units of 10^{37} ergs s^{-1}: 2.2 (N4), 1.9 (N5), 1.6 (N6), 1.3 (N7), 3.6 (N8), and 2.4 (N9). The uncertainties in these estimates are at least a factor of 3 since the actual absorbing columns are unknown. This uncertainty is, alas, comparable to some of the uncertainties in L_{bol} obtained for the brightest sources.

Alternatively, luminosities can be estimated from the count rate and assuming a (blackbody) temperature and a column density. The weakest supersoft source detected has an observed luminosity of 2×10^{36} ergs s^{-1} assuming an 80 eV blackbody spectrum and a column of $N_H = 8 \times 10^{20}$ cm^{-2}. This corresponds to $L_{bol} \sim 1.3 \times 10^{37}$ ergs s^{-1}. L_{bol} increases to 5.2×10^{37} ergs s^{-1} if the assumed temperature is lowered to 50 eV.

Temperatures cannot be so easily estimated, but they are most probably of the order of 40–50 eV since higher temperature sources are expected to be rare based on theoretical models of supersoft sources (see § 5) and cooler sources are difficult to detect with *Chandra* ACIS. Even an intrinsically bright ($L_{bol} = 10^{38}$ ergs s^{-1}) blackbody source with $T_{eff} = 25$ eV and moderate absorbing column (2 times Galactic) produces only 24 counts in the BI device and would be undetectable in the FI chips.

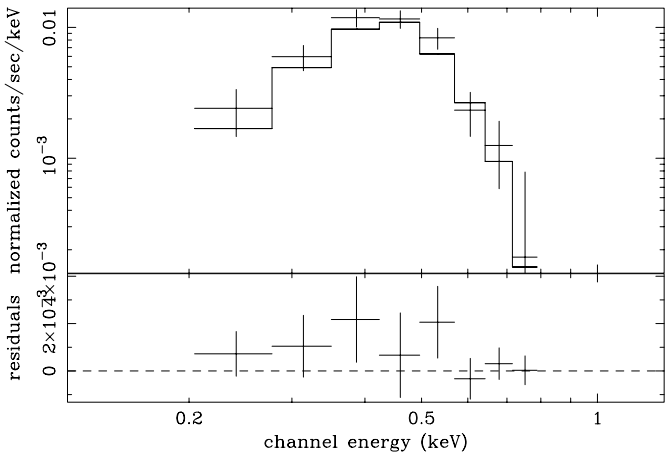

FIG. 7.—*Top*: Observed spectrum of source N3 (*symbols*), best-fit WD LTE atmosphere model spectrum with solar abundance metals, and solar abundance photoelectric absorption (*solid line*). Spectrum and model have been rebinned to show structure. *Bottom*: Fit residuals.

4. X-RAY TIMING ANALYSIS

4.1. *Short-Term Variability*

The 50 ks *Chandra* light curves of the brightest three supersoft source candidates are presented in Figure 8. Detected events have been binned on 1000 s intervals.

The observation was of sufficient duration that the Kolomogorov-Smirnov statistic can be evaluated for the brightest sources to test the hypothesis that the sources are constant. The test shows that sources N1 and N2 are variable at high confidence but that the remaining sources contain insufficient data to be conclusive. Power spectra were also generated for the brightest sources to search for pulsations or other periodic behavior. Only source N1 had sufficient signal to obtain significant results. No periodicity was detected.

An additional 2.4 ks ACIS-S imaging observation of M81 obtained on 2000 March 21, 47 days prior to the 50 ks observation, was acquired through the *Chandra* X-ray Center data archive. Source N1 is the only supersoft source candidate with a sufficient number of counts in this short exposure for analysis. The light curve of source N1 during this observation, binned on 300 s intervals, is shown in Figure 9. Also shown are the corresponding light curves in the energy bands 0.2–0.5 and 0.5–1.0 keV and the time dependence of the background during the observation. The source brightness declines from a maximum at the beginning of the observation to a statistically insignificant level within ~900 s and remains at this low level for the remainder of the observa-

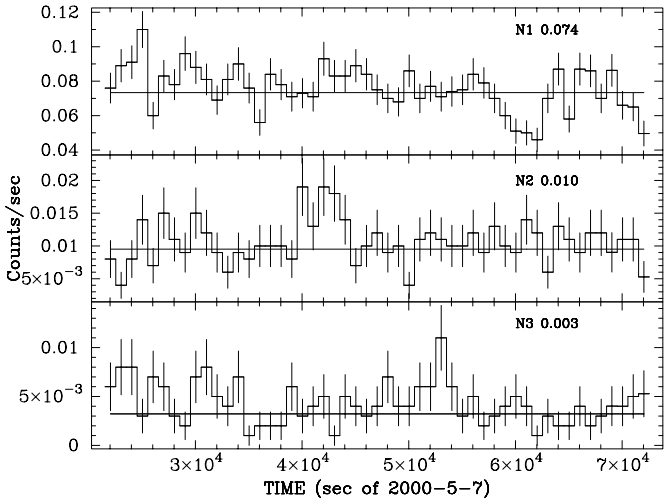

FIG. 8.—*Chandra* light curve of the brightest supersoft source candidates binned on 1000 s intervals. All standard-grade events in the 0.2–2.0 keV bandpass, within valid good-time intervals and within the same spatial regions as used for spectral analysis, are included. Error bars represent 1 σ statistical uncertainties. Background contributions are negligible: typical background count rates are 10^{-6} counts s^{-1} $pixel^{-1}$. Labels denote source number and average count rate obtained by fitting a constant to the data (shown as horizontal lines through the data).

tion. No other (bright) source displayed similar changes in X-ray flux during the 2.4 ks observation.

The dramatic drop in flux suggests an eclipse event. The observation interval is too short to establish a brightening of the source signifying the end of the eclipse (the observation ended 100 s into the last interval, and this interval contains four counts, one of which is probably a background photon based on its PI value). No similar feature is detected in the longer *Chandra* observation, and no similar feature can be seen in the relatively poor signal-to-noise *ROSAT* data discussed below.

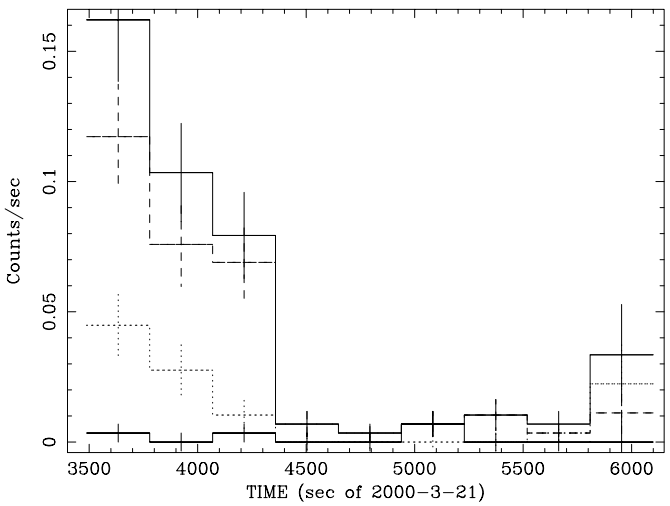

FIG. 9.—*Chandra* 2 ks light curve of source N1 binned on 300 s intervals. The uppermost curve includes all standard-grade events in the 0.2–2.0 keV band, the next lower curve represents the 0.5–1.0 keV band (*dashed line*), followed by the 0.2–0.5 keV band (*dotted line*). The lower curve represents the nearby background scaled by the ratio of the source to the background area. Error bars represent 1 σ statistical uncertainties.

Assuming that the drop in flux signals the onset of an eclipse of an $\sim 1\ M_\odot$ compact object, that Roche-lobe overflow from the companion is occurring, that the eclipse duration exceeds 1600 s, and that no eclipse occurs during the 50 ks exposure, weak constraints on the orbital elements of any binary system can be derived. These constraints are easily met by massive companions ($\gtrsim 3\ M_\odot$) that have evolved off the main sequence. Systems in this mass range have periods greater than $\sim$1.6 days and eclipse fractions of order of 15%. Missing an eclipse is then quite likely, although witnessing the onset of an eclipse in a short exposure would be fortuitous. Furthermore, such companion stars should be visible in the *HST* images (§ 2.2).

A more likely scenario for supersoft sources is a slightly evolved main-sequence donor in the mass range 1.3–2.5 $M_\odot$ (van den Heuvel et al. 1992) or a "helium Algol" with a companion of a few solar masses at the onset of He accretion (Iben & Tutukov 1994; Yungelson et al. 1996). Orbital periods range from 10 to 30 hr for the main-sequence donor scenario and less than 20 hr for the He-accreting systems (Yungelson et al. 1996). There is at best a one in three chance that no eclipse is observed during a 50 ks (13.9 hr) observation of systems with a 30 hr period, and the probability decreases for the shorter period systems. Thus, although an eclipse cannot be excluded by the X-ray observations, it is not very likely.

Assuming that the source is exiting an eclipse phase during the last $\sim$300 s of the short exposure, then the eclipse lasts only of order of 1800 s. The orbital period must then be of the order of a few hours only since $\sim$15% of the period is spent in eclipse. A period this short could not be missed in the 50 ks observation.

Alternatively, nuclear burning on the surface of a WD may be occurring through weak shell flashes that either cause expansion that quenches burning or expel material that obscures the underlying atmosphere as it cools with more violent flashes followed by a larger flux decline. This may explain the Figure 9 light curve where the X-ray flux is roughly a factor of 2 brighter during the onset of the observation than the average value observed during the 50 ks observation (Fig. 8). Fitting an exponential to the first 1000 s of this light curve gives an *e*-folding timescale of $\sim$350 s. This is comparable to the sound crossing time over the surface of a WD for reasonable estimates of the sound speed in the burning layer. A change in accretion rate may also trigger large excursions in the X-ray brightness. Southwell et al. (1996) have suggested that this mechanism may explain the factor of $\sim$20 rise in X-ray flux observed (Schaeidt, Hasinger, & Trümper 1993) in the supersoft source RX J0513.9−6951. However, the timescale for contraction of the photosphere leading to the required change in $T_{\rm eff}$ is of the order of days (Livio 1992). RX J0513.9−6951 is probably a low-mass WD system with a correspondingly low X-ray luminosity (Greiner 2000b) far below that observed for source N1.

Interestingly, the spectrum is substantially harder and the brightness is higher during the bright portion of the 2.4 ks observation compared to the 50 ks observation. There is even some flux above 1.0 keV in the 2.4 ks data. The mean photon energy during this bright phase is $\sim$730 eV, while during the 50 ks observation the mean is $\sim$475 eV (Fig. 5). Part of the spectral hardening, including most of the flux above $\sim$1.1 keV, is caused by pileup in the high-rate data. Nevertheless, the spectrum is definitely harder (or hotter in

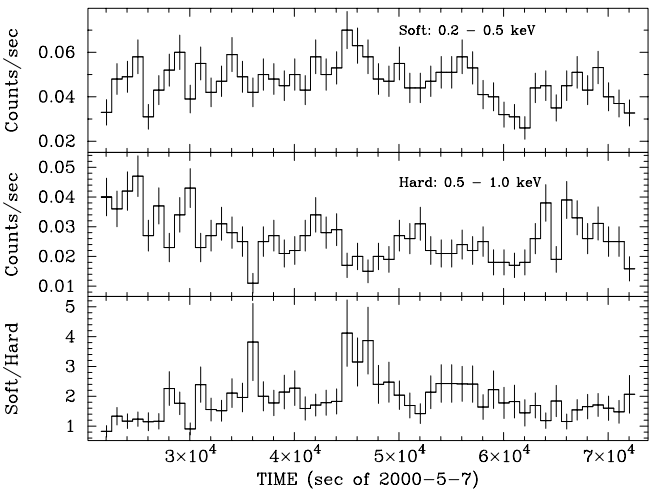

FIG. 10.—*Chandra* 50 ks light curve of source N1 in the 0.2–0.5 keV (*top*) and the 0.5–1.0 keV (*middle*) energy bands binned on 1000 s intervals. The bottom panel displays the ratio of the two energy bands. Error bars represent 1 σ statistical uncertainties.

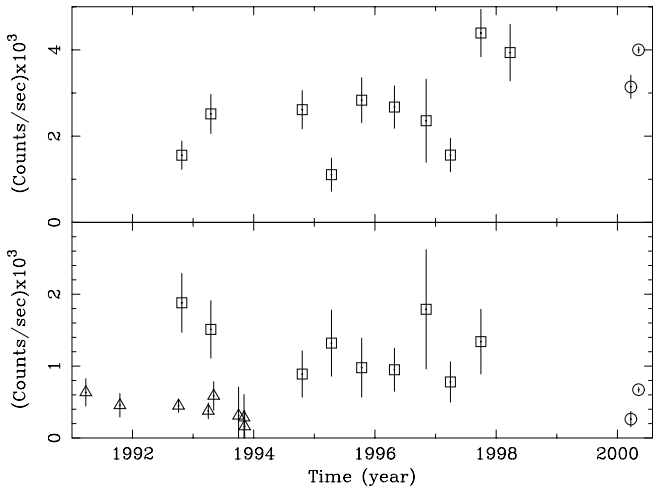

FIG. 11.—Combined *ROSAT* and *Chandra* light curves for source N1 (*top*) and N2 (*bottom*). Count rates have been scaled to *ROSAT* HRI count rates assuming the spectral parameters derived in § 3 from the 50 ks *Chandra* data. *ROSAT* HRI data are marked with squares, *ROSAT* PSPC data with triangles, and *Chandra* data with circles. Errors denote 1 σ statistical uncertainties. Labels denote average observed count rates.

the context of blackbody spectral models) during this bright phase. There is no clear signature of increasing absorption as the source enters the low-rate region of the 2.4 ks light curve, as would be expected in the onset of an eclipse. No other source shows a similar harder spectrum during the 2.4 ks observation.

The other alternative discussed previously in the context of spectral models for source N1 is X-ray emission from an accretion disk around a midmass black hole. Variability on many timescales is observed in both massive black holes (AGNs) and stellar mass black holes (X-ray transients). Variability is generally caused by instabilities in the disk structure and changes in the accretion flow and is usually accompanied by spectral evolution among high soft states and low hard states. The 50 ks light curve of source N1 in each of two energy bands is shown in Figure 10 along with the ratio of the soft band to the hard band. This shows that source N1 varies differently in different energy bands, but it does not help distinguish between standard supersoft source and midmass black hole scenarios.

4.2. *Long-Term Variability*

The fluxes observed by *Chandra* suggest that the brightest four or five supersoft source candidates may be detectable in archival *ROSAT* observations of the field. M81 was observed nine times by *ROSAT* PSPC over the interval from 1991 March to 1994 April and 11 times by *ROSAT* HRI from 1992 October to 1998 April. Source N1 is present in *ROSAT* HRI images but is too near the bright nucleus of M81 to be resolved in *ROSAT* PSPC data. Source N2 is clearly present and isolated from other X-ray sources in both PSPC and HRI observations. Source N3 is confused with a bright nearby object in both *ROSAT* instruments. Source N4 is likewise too near the nucleus for positive detection. Source N5 is marginally detected at the 2.8 σ level in the longest of the HRI exposures. This corresponds to a *Chandra* luminosity of $\sim 2 \times 10^{37}$ ergs s^{-1}, consistent with a constant source luminosity between the two observations. The remaining sources are too weak to be detected at a reasonable confidence level. The entire *ROSAT* data set has been independently analyzed by Immler & Wang (2001). *Chandra* source N1 is within 3.″2 of HRI source H25 of Immler & Wang (2001) and is listed as a variable source with no other comment. Source N2 is within 3.″3 of HRI source H36, which is coincident with PSPC source P44. Source P44 is a soft source based on its PSPC hardness ratios (Immler & Wang 2001). No other *Chandra*-detected supersoft source candidate is among the *ROSAT* sources identified by Immler & Wang (2001).

The combined *ROSAT* HRI, PSPC, and *Chandra* light curves of sources N1 and N2 are displayed in Figure 11. Here the average count rate of each individual observation is shown combined to form each data point. The *Chandra*- and *ROSAT* PSPC–observed count rates have been scaled to *ROSAT* HRI–observed count rates using the PIMMS tool (Mukai 1993) and assuming spectral properties for the two sources as derived in § 3. This scaling can account for some of the disparity seen, for example, in the lower panel of Figure 11 (source N2), where the PSPC data and the two *Chandra* points are lower than the intervening *ROSAT* HRI fluxes. Nevertheless, both sources are clearly present in the data spanning more than 7.5 yr. As discussed in the next section, this fact limits the possibility that these sources could be classical novae.

5. DISCUSSION

Supersoft sources are a well-established class of X-ray–emitting object. Of the 19 well-studied systems (see, e.g., Greiner 2000a), all within the Galaxy or the Magellanic Clouds, nine are accreting WD close binary supersoft sources (CBSSs) that are nuclear burning accreting material in a steady state, four are classical or recurrent novae, three are symbiotic systems, and one is a planetary nebula nucleus. The common source of X-ray emission among these sources is nuclear burning of either accreting material (in a steady state or in a nova flash) or residual fuel (following, e.g., the formation of a planetary nebula).

The assumption that all supersoft sources result from nuclear burning on WD stars is adopted here for purposes of discussion. Two questions to be addressed are as follows: (1) Are the observed population and its distribution within M81 consistent with this theory? (2) Are the observed X-ray properties of the individual sources consistent with previously observed members of this rather heterogenous class (and, if so, which ones)?

5.1. *The M81 Population of Supersoft Sources*

Nine supersoft source candidates have been identified in M81 based on broadband X-ray colors. All are located on the S3 device. Four of these are located in the bulge of M81, and the remainder are aligned with the spiral arms, with the exception of one object in the interarm disk region. The bulge comprises 30% of the area of the S3 device;[6] thus 2.7 of the nine supersoft sources should occur in the bulge if the spatial distribution were uniform on S3. However, 54 of the 97 X-ray sources of all types on S3 are located in the bulge (Tennant et al. 2001), and therefore five supersoft sources would be expected there if the supersoft sources follow the general distribution of X-ray sources. Twenty-one of the 43 disk X-ray sources are aligned with the spiral arms, while four of the five supersoft disk sources are on the arms.

The observed properties of the supersoft sources in M81 favor high-mass WD systems ($M_{\rm WD} \sim 1.0\ M_{\odot}$) and hence a younger population of progenitor stars (zero-age main-sequence mass $\sim 7\ M_{\odot}$). This favors locations near star-forming regions such as spiral arms. Conversely, the interstellar absorption is relatively higher in the spiral arms than in the disk or bulge, which would tend to obscure the lowest temperature supersoft sources. Indeed, the two supersoft sources located on the spiral arms with sufficient counts for spectral fitting (N2 and N3) have relatively high X-ray–absorbing columns and temperatures of 50–60 eV.

Objects in the bulge are expected to be an older population (>9 Gyr; see, e.g., Kong et al. 2000) except in the central $\sim 50''$, where an enhancement in recent star formation activity is suggested by UV (Hill et al. 1992; Reichen et al. 1994) and Hα (Devereux et al. 1995) imaging and consistent with the concept of gas infall toward the center of M81. This may have begun as recently as $\sim$400 Myr ago as a result of an encounter with NGC 3077 (Thomasson & Donner 1993) or M82 (de Grijs, O'Connell, Gallagher 2001). All the bulge supersoft source candidates lie outside this central region and appear to have relatively low absorbing columns consistent with the lack of gas and dust. The standard supersoft source model (van den Heuvel et al. 1992) requires companion stars in the mass range 1.3–2.5 $M_{\odot}$ to maintain steady nuclear burning of accreting H on the surface of the WD. Stars of this mass range evolve from the main sequence on timescales of order of several 10^8 to more than 10^9 yr, and so the required accretion could be occurring in the current epoch in the bulge if the donor stars were formed in an encounter.

How many supersoft sources are expected in the 50 ks *Chandra* observation? Di Stefano & Rappaport (1994) estimated the number of supersoft sources in external galaxies observable by *ROSAT* by carefully accounting for the effects of interstellar absorption on an assumed parent population taken from the work of Rappaport et al. (1994b). The parent population was that of systems whose luminosities and temperatures matched the steady-burning regime computed by Iben (1982). This omits everal classes of supersoft sources including wind-driven symbiotic systems, novae, and recurrent novae. Nevertheless, it is possible to apply the basic approach of Di Stefano & Rappaport (1994) to the *Chandra* observation of M81. Scaling from their estimate of the total population of supersoft sources in M31 by the ratio of blue luminosities (i.e., assuming that supersoft sources contain massive WDs and hence evolved from a young stellar population [Motch, Hasinger, & Pietsch 1994; Di Stefano & Rappaport 1994]), a total of 1700 supersoft sources are expected in M81.

To estimate the fraction detectable by *Chandra*, the population distributions in temperature and bolometric luminosity as derived by Rappaport et al. (1994b) can be roughly approximated by normal distributions with means $T = 24$ eV and $L = 3 \times 10^{37}$ ergs s^{-1} and standard deviations of 13 eV and 8.5×10^{36} ergs s^{-1}, respectively (see also Fig. 3 of Di Stefano & Rappaport 1994).

By randomly sampling values of T and L from these two independent distributions, assuming a blackbody spectrum and a modest column of $N_{\rm H} = 8 \times 10^{20}$ cm^{-2} (twice the Galactic value), and using the PIMMS software tool (Mukai 1993), the predicted *Chandra* observed count rate distribution can be accumulated. Assuming 20 counts in a 50 ks observation as a detection threshold, only 1% of the supersoft sources in M81 should be detectable with the BI device S3.

Since the viewing field of S3 encompasses 23% of the D_{25} area of M81, approximately four of the 1700 supersoft sources in the parent population should be detected in the 50 ks observation on S3. This is consistent with the observed population of nine sources in light of the large uncertainties involved, including a factor of 2 uncertainty in the normalization of the parent population (Di Stefano & Rappaport 1994), and the neglect of other classes of supersoft source systems by these authors (Yungleson et al. 1996).

The simulation also shows that only systems with temperatures $T \gtrsim 40$ eV and bolometric luminosities $\sim 2 \times 10^{37}$ ergs s^{-1} are likely to be detected by *Chandra*. This result can be compared to the distribution of temperatures and luminosities reported in Greiner (2000a) for 21 supersoft sources (two of which have not been optically classified) and to the nine supersoft sources discovered in M81. Figure 12 shows this comparison. (For brevity, it has been assumed here that the six weakest supersoft sources in M81 all have temperatures of 45 eV; see § 3.4.) The distributions of the Greiner (2000a) sample are clearly broader than predicted or observed for M81. This is a consequence of the greater diversity of local environments in which these sources are found and the dissimilar instruments used to investigate them. The peaks of the observed M81 distributions in temperature and luminosity coincide with the predicted distribution, but these peaks are dominated by the weak sources and are, therefore, highly uncertain. The bright observed sources are, however, located at higher temperatures and luminosities than expected.

[6] The bulge is defined here as the region interior to the inner Lindblad resonance at radius 4 ± 0.2 kpc (Kaufman et al. 1989 and references therein). This is larger than the bulge radius (2.55 kpc) adopted by Tennant et al. (2001), resulting in 13 more X-ray sources within the bulge.

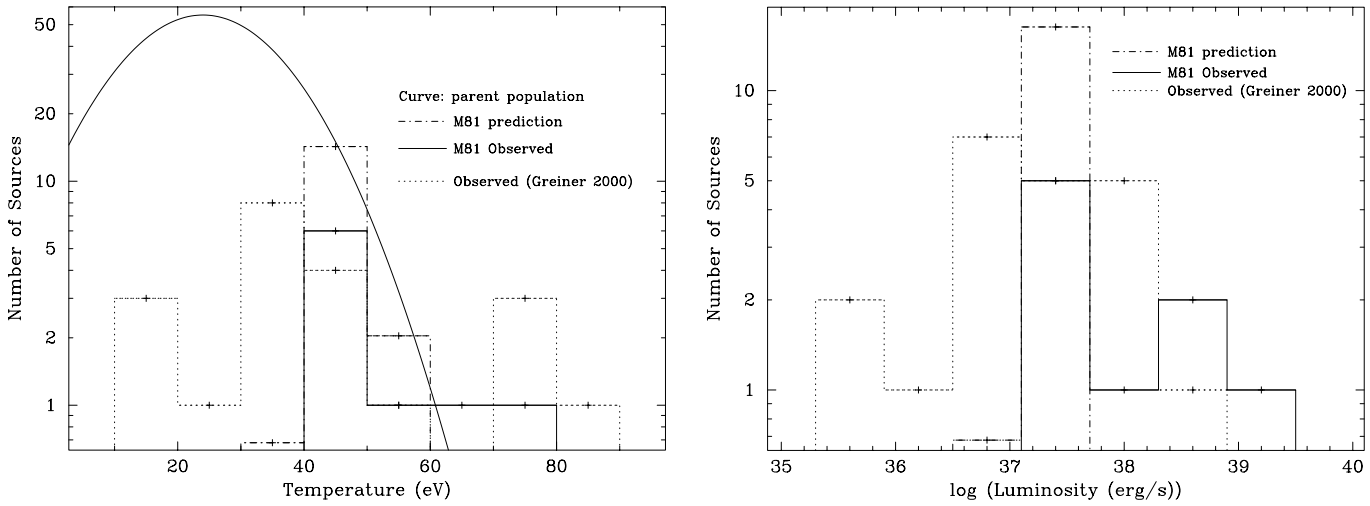

FIG. 12.—Distribution of supersoft source systems over effective temperature (*left*) and bolometric luminosity (*right*). Shown are the predicted and observed distributions for the galaxy M81 (see text) and the distribution of known sources in the Galaxy and Magellanic Clouds as cataloged by Greiner (2000a). The M81 predicted distributions assume that the sources are distributed normally over both temperature and luminosity. This normal distribution is the curve in the left-hand panel. For clarity, the corresponding distribution is omitted from the right-hand panel since it appears as a narrow asymmetric curve centered on 3×10^{37} ergs s^{-1} in the logarithmic scaling used here.

5.2. *The Nature of Individual M81 Supersoft Sources*

5.2.1. *Source N1*

By far the brightest supersoft source candidate in the sample lies within the bulge of M81 approximately 52″ from the nucleus. Its spectrum is well fitted with a simple blackbody model of 78–86 eV ($T \sim 9 \times 10^5$ K) with a modest absorption ($N_{\rm H} \sim 6 \times 10^{20}$ cm^{-2}) resulting in an implied bolometric luminosity exceeding 10^{39} ergs s^{-1}. Although the bolometric luminosity is highly uncertain, even the observed luminosity exceeds the Eddington limit for a Chandrasekhar mass WD.

The brightest well-studied supersoft sources are typically novae or recurrent novae with peak bolometric luminosities often exceeding 10^{38} ergs s^{-1}. One of the best examples is U Sco. Kahabka et al. (1999a) investigated *BeppoSAX* observations of this recurrent nova taken ~20 days after the peak of the most recent optical outburst. They find a temperature of $\sim 9 \times 10^5$ K and a bolometric luminosity of up to 2×10^{38} ergs s^{-1} from a combination of non-LTE atmosphere models and an optically thin thermal emission component, assumed to arise from a wind, added to fit the ~1–2 keV portion of the observed spectrum.

Although source N1 has X-ray properties similar to those of U Sco, it is unlikely that source N1 is a nova. Novae occur in systems with relatively low mass transfer rates where a layer of fuel is accumulated for a period of time before compressional heating causes ignition. The mass of the accumulated layer increases with decreasing WD mass. Consequently, the X-ray light curves evolve slowly, lasting up to 10 yr or so, in systems with low-mass WDs. The luminosity is proportional to the WD mass $M_{\rm WD}$, $L_{\rm bol} \sim 1.8 \times 10^{38}(M_{\rm WD} - 0.26)$ ergs s^{-1}, assuming H accretion, where $M_{\rm WD}$ is measured in solar units (Iben & Tutukov 1989). Thus, the luminosity is low for these long-lived low-$M_{\rm WD}$ novae, and the recurrence time between events is very long. Conversely, systems containing high-mass WDs, such as inferred for U Sco, have a higher peak luminosity but are short-lived X-ray sources (~0.1 yr; see, e.g., Kato 1997). The recurrence times are also shorter but are still of the order of years and therefore inconsistent with the observed light curve of source N1. (Note that the short- and long-term variations observed in the X-ray light curve of source N1 are better described as transience or variability in contrast to recurrence as applied to novae.)

At higher accretion rates is a regime of steady state burning of accreting material. The maximum luminosity in the steady-burning regime is $L_{\rm bol} = 2.3 \times 10^{38}(M_{\rm WD} - 0.5)$ ergs s^{-1} and occurs at the maximum accretion rate $\dot{M} = 7.8 \times 10^{-7}(M_{\rm WD} - 0.5)\ M_\odot$ yr^{-1} (Iben 1982, again assuming H-rich accretion). The highest temperatures, up to ~85 eV, are obtained by the highest mass WDs, as are the highest luminosities. However, an accretion rate of $\sim 5 \times 10^{-6}\ M_\odot$ yr^{-1} is needed to obtain the bolometric luminosity inferred for source N1 assuming steady burning. At such high accretion rates, however, the photospheric radius expands to red giant dimensions, only a fraction of the fuel is consumed, and the X-ray emission, formed in a thin layer at the base of the envelope, is hidden by the overlying material. The burning may instead drive a strong, opaque wind (Hachisu, Kato, & Nomoto 1996). If the outcome of a high mass transfer rate is the formation of an envelope, then this system should be observable optically as a hot giant or red giant star, contrary to the *HST* observations (§ 2.2), and not as a strong X-ray source. If the accretion drives a wind, then the photospheric temperature is only $T \sim 10^5$ K. However, if the accretion rate *decreases*, the wind mass-loss rate will decrease as will the effective photospheric radius. Regions closer to the burning layer will become exposed, and the X-ray temperature and X-ray luminosity will increase dramatically (Hachisu et al. 1996). The subsequent evolution of systems of this type were not followed by Hachisu et al. (1996).

If the accreting material is He-rich, then the system can sustain a higher mass transfer rate while remaining in the steady nuclear-burning regime (Iben & Tutukov 1989). The increase in mass transfer rate by roughly an order of magnitude translates into only a factor of 2 or so higher luminosity because of the lower specific energy generation rate of He relative to H so that the maximum luminosity is

$L_{\rm bol} \sim 4.6 \times 10^{38}(M_{\rm WD} - 0.58)$ ergs s^{-1} (Iben & Tutukov 1989). Although He-rich LTE white dwarf atmosphere models failed to provide a satisfactory fit to the observed spectrum, He-rich accretion remains an attractive scenario for source N1 because the Eddington limit luminosity for He accretion is twice that for H. Helium accretion can occur during a second phase of mass transfer to the compact star when the companion has exhausted He in its core (Iben & Tutukov 1994). The donor star in this scenario is either the nucleus of an early asymptotic giant branch or an evolved He star remnant with a CO core. Under appropriate conditions, this mass transfer can be conservative (Iben & Livio 1993) instead of lost in a common envelope process (Iben & Tutukov 1985). The initial mass of the donor star tends to be rather large in this scenario, $\sim$6.5–9.5 $M_\odot$ for steady burning, so that such systems should be rather rare in the old population of bulge stars in M81. Helium tends to burn explosively (Sion & Starrfield 1993) unless the helium layer can be maintained at a high temperature (José, Hernanz, & Isern 1993). A series of weak He shell flashes may occur for systems near the stability limit producing luminosities of order of $\sim 4 \times 10^{38}$ ergs s^{-1} and temperatures of $\sim$70 eV (Iben & Tutukov 1994). These systems tend to have shorter than $\sim$20 hr orbital periods (Yungelson et al. 1996), comparable to or less than those of subgiant donors in H-accreting systems and of main-sequence stars losing mass on a thermal timescale ($\sim$1 day orbital periods; van den Heuvel et al. 1992). Another channel for He accretion is a semidetached double degenerate system in which the secondary is a helium WD (Iben & Tutukov 1989). Such a system must have an orbital period of order of minutes (Verbunt & van den Heuvel 1995).

In short, none of the standard nuclear-burning WD scenarios predict luminosities as high as that inferred for source N1. However, theoretical treatments have not rigorously explored the behavior of these systems in regimes beyond the stability limit. Other alternatives exist. Neutron star binaries often exhibit a luminous thermal component, although rarely as soft as observed here (and hence one of the original motivations for the nuclear-burning WD scenario for supersoft sources; van den Heuvel et al. 1992). One exception is the Be/X-ray binary RX J0059.2$-$7138 with $T_{\rm eff} \sim 36$ eV (Hughes 1994), although this source is accompanied by a strong power-law component extending the spectrum beyond the *ROSAT* band. Weakly magnetized neutron stars, such as the X-ray burst sources, tend to have correspondingly weak power-law spectral components, but they also have high characteristic temperatures during the burst phase (see, e.g., Lewin, van Paradijs, & Taam 1995). Similarly, typical black hole binaries display a "soft" component with a characteristic temperature greater than 1 keV and a hard power-law component.

A completely different scenario that may explain the observed X-ray properties of source N1 is X-ray emission from an optically thick accretion disk surrounding a mid-mass black hole. The most attractive feature of this model is that the implied bolometric luminosities derived here are a small fraction of the Eddington limit. The observed X-ray spectrum is consistent with that from the innermost disk radius assuming that the central object has a mass $M_{\rm BH} \sim 1200/(\cos i)^{1/2}$. While no objects in this mass range have been confirmed, invoking the Eddington limit to X-ray bright sources has led to suggestions of masses in excess of 10–100 $M_\odot$ in many instances (see, e.g., Makishima et al. 2000) and as high as $\sim$700 $M_\odot$ in the case of a luminous source in M82 (Kaaret et al. 2001; Matsumoto et al. 2001).

5.2.2. *Source N2*

Source N2 has a distinct edge at $\sim$870 eV well fitted by O VIII absorption in the LTE atmosphere model. This feature is commonly found in the hotter supersoft sources such as the LMC source CAL 87. Ebisawa et al. (2001) find a temperature of 75 eV for CAL 87 from *ASCA* observations with an absorbing column comparable to that obtained here for source N2 ($N_{\rm H} \sim 2 \times 10^{21}$ cm^{-2}).

Parmar et al. (1997) report that *BeppoSAX* observations of CAL 87 are equally well fitted with either blackbody, LTE, or non-LTE (NLTE) atmosphere models with temperatures ranging from 42 eV for the blackbody fits to 57 and 75 eV for their LTE and NLTE models, respectively. The blackbody model implies $L_{\rm bol} \sim 4 \times 10^{38}$ ergs s^{-1}, but the LTE and NLTE fits are consistent with more modest luminosities, $\sim(3\text{–}5) \times 10^{36}$ ergs s^{-1}. Including the O VIII absorption edge increases the blackbody temperature and decreases the bolometric luminosity to values similar to their NLTE models.

This trend is opposite to the results reported here for source N2: blackbody models predict higher temperatures than the LTE models and bolometric luminosities comparable to or lower than the LTE models. The best-fit model, LTE with 1% of solar metal abundance, has a temperature of 67 eV and a hydrogen column density of 1.6×10^{21} cm^{-2} very similar to CAL 87. The observed luminosity is 3.9×10^{37} ergs s^{-1} and $L_{\rm bol} \sim 5.3^{+4.8}_{-2.1} \times 10^{38}$ ergs s^{-1}, much higher than the models of Parmar et al. (1997) but consistent (within the large uncertainties) with the highest luminosity reported by Ebisawa et al. (2001) for CAL 87.

CAL 87 is a close binary system that exhibits eclipses with a period of 10.6 hr. The eclipses are visible as shallow dips in the X-ray light curve. Small-amplitude variability of this kind cannot be distinguished in the relatively low-quality light curve of source N2.

5.2.3. *Source N3*

This source is also relatively highly absorbed but considerably cooler than the two brightest sources with $T_{\rm eff} \sim 50$ eV. This value is more typical of many of the well-studied supersoft sources (Fig. 12; see also Greiner 1996, 2000a), such as the CBSSs CAL 83 and 1E 0035.4$-$7230. Parmar et al. (1998) report that acceptable fits can be achieved with blackbody, LTE, or NLTE atmosphere models applied to *BeppoSAX* observations of CAL 83. Their resulting temperatures are $\sim$45 eV for the blackbody and LTE models and $\sim$33 eV for their NLTE fits. As with source N3 (§ 3.3), Parmar et al. (1998) report that the low temperature and consequent lack of strong absorption edges do not allow a distinction to be made among the models (see also Fig. 4). *BeppoSAX* and *ROSAT* observations of 1E 0035.4$-$7230 (Kahabka et al. 1999b) again do not allow either blackbody, LTE, or NLTE models to be discounted, although in this case a feature ascribed to C V and C VI absorption is evident. Temperatures derived by Kahabka et al. (1999b) range from $\sim 40 \pm 13$ eV from their blackbody fits to $\sim 28 \pm 4$ eV from their NLTE model fits to 1E 0035.4$-$7230. Both CAL 83– and 1E 0035.4$-$7230–derived bolometric luminosities are of order of a few times 10^{37}, roughly an order of magnitude

lower than the best-fit values derived here for source N3, although within the large uncertainties in the latter.

5.2.4. *Source N4 and N5*

Although little can be said about the X-ray properties of these two sources beyond their broadband classification as supersoft source candidates, these objects may be similar to the LMC source CAL 83.

Sources N4 and N5 are spatially coincident with objects ID 68 and 116, respectively, in the list of [O III] λ5007 sources observed by Jacoby et al. (1989). This emission line is also prominent in the optical images of CAL 83 (Remillard et al. 1995) and is attributed there to ionization in the interstellar medium by a large UV and soft X-ray photon flux from the central source. Rappaport et al. (1994b) modeled the ionized regions surrounding supersoft sources and calculated resulting optical line intensities. The strongest predicted lines are the [O III] λ5007 and He II λ4686 lines. Adopting the foreground extinction to M81 from Jacoby et al. (1989), their observed [O III] λ5007 fluxes are consistent with those expected from the supersoft source models. For example, the λ5007 flux from object ID 116 is $\sim 4 \times 10^{-16}$ ergs cm^{-2} s^{-1}, while Rappaport et al. (1994a) predict 1.6×10^{-16} ergs cm^{-2} s^{-1} and 2.3×10^{-15} ergs cm^{-2} s^{-1} from models with intrinsic luminosities of 10^{37} and 10^{38} ergs s^{-1}, respectively, and source temperatures of 4×10^5K.

Parmar et al. (1998) find a temperature $T_{\rm eff} \sim 30$–50 eV for CAL 83 and $L_{\rm bol} \sim 4 \times 10^{37}$ ergs s^{-1}. These values are within the estimated values for sources N4 and N5.

A PN cannot be excluded based on the X-ray and [O III] fluxes of sources N4 and N5. The central stars of PNs can have luminosities as high as those inferred for sources N4 and N5, but only the most massive central stars are hot enough to be detected in soft X-rays (see, e.g., Paczynski 1971). This is the case for the SMC supersoft source 1E 00056.8−7154. This source is coincident with PN N67 (Wang 1991) but is anomalously X-ray bright for a PN ($T_{\rm eff} \sim 38$ eV, $L_{\rm bol} \sim 2 \times 10^{37}$ ergs s^{-1}; Brown et al. 1994; Heise et al. 1994). Unfortunately, no obvious spectroscopic distinction between PNs and supersoft sources has been identified (Di Stefano, Paerels, & Rappaport 1995).

5.2.5. *Other Sources*

The X-ray evidence in support of a supersoft source nature of the remaining candidates is based entirely on their X-ray colors. Their spectra and light curves are of insufficient quality for detailed analysis.

Since there is no long-term X-ray light curve for these sources, their identification as novae cannot be ruled out. The rate of nova occurrence in M81 is roughly 20 yr^{-1} (Della Valle & Livio 1994), and, as discussed above, X-ray lifetimes range from months for the brightest sources up to $\sim$10 yr. For the values of $L_{\rm bol}$ estimated in § 3, 10^{37}–4×10^{37} ergs s^{-1}, the corresponding WD masses are low, $M_{\rm WD} \sim 0.3$–$0.5\ M_\odot$. These masses correspond to long-lived novae, typically radiating as a (very soft) X-ray source for $\sim$7 yr for $M_{\rm WD} = 0.6\ M_\odot$ (Kato 1997).

Visual magnitudes of novae can be as high as $m_V \sim 22$–23 at the distance of M81, but the visible light rapidly declines after maximum light as the spectrum hardens and the X-ray flux rises. A 0.6 $M_\odot$ WD nova, for instance, only becomes X-ray visible $\sim$4 yr after optical outburst.

The weak supersoft source candidates could also be steady-burning CBSS systems. The estimated $L_{\rm bol}$ corresponds to a range of WD masses from $M_{\rm WD} \sim 0.7$ to $\lesssim 1.0$. However, WDs in this mass range should be considerably cooler ($T_{\rm eff} \lesssim 40$ eV) than the 40–50 eV temperatures suggested by the instrumental selection effect. Below $M_{\rm WD} \sim 0.65\ M_\odot$, the photospheric radius expands in the steady nuclear-burning case and $T_{\rm eff}$ plummets (Iben 1982). Thus, only a narrow range of masses is possible for the weak supersoft sources if they are steadily burning their accreted hydrogen.

Another evolutionary channel leading to the formation of a supersoft source is wind-driven accretion in symbiotic systems (Sion & Starrfield 1994). These systems can undergo H shell flashes, reach luminosities of order of $\sim 10^{37}$ ergs s^{-1}, and remain at this plateau for $\sim$250 yr in some circumstances. For many of the low-mass WDs modeled by Sion & Starrfield (1994), the flashes are weak, the envelope radius remains compact, and the resulting photospheric temperature is relatively high. However, the maximum temperatures achieved were $T_{\rm eff} \sim 20$ eV. The supersoft source SMC 3 (RX J0048.4−7332) is a symbiotic nova of this type. Jordan et al. (1996) derive a luminosity $L_{\rm bol} \sim 4 \times 10^{37}$ ergs s^{-1}, a temperature of 22 eV, and a mass of $\sim 0.8\ M_\odot$ for this object. The weak supersoft source candidates are unlikely to be symbiotic systems because of the difficulty of detecting objects of such low temperatures in M81 with *Chandra*. An archival *Chandra* observation of AG Dra, for instance, detects very little flux above $\sim$0.3 keV.

6. SUMMARY AND PROSPECTS

6.1. *Chandra Observations of M81*

An important part of the *ROSAT* legacy has been the identification of supersoft sources as a phenomenologically distinct class of X-ray–emitting object. The *Chandra X-Ray Observatory* affords an excellent opportunity to extend the study of supersoft sources to other nearby galaxies.

As a first step, the population of supersoft source candidates discovered in M81 has been investigated. The number of supersoft sources detected and their spatial distribution are consistent with population synthesis estimates. X-ray spectral analysis shows the M81 sources are qualitatively similar to previously studied supersoft sources, although the brightest M81 sources tend to be hotter and more luminous than is typical of the class. This was shown to be, in part, a natural consequence of the higher sensitivity of *Chandra* to the high-temperature region of the supersoft source distribution.

Bolometric luminosities deduced here from the spectral fits often exceed the Eddington limit for spherical accretion onto a 1.4 $M_\odot$ star. Such extreme luminosities lie beyond the previously observed distribution of supersoft sources and, more importantly, cannot be reconciled with prevailing theories for supersoft sources as WDs powered by stable, steady state, surface nuclear burning. But the study of supersoft sources with *Chandra* is still in its infancy. Important uncertainties remain. As in the *ROSAT* era, spectral modeling remains problematic. Simple blackbody models, like those used in this work, are known to greatly overestimate bolometric luminosities in some cases. LTE model atmospheres, also applied here, are appropriate when a well-defined photosphere is present, such as in the high-den-

sity gradient at the surface of a WD. Even this model fails when the nuclear burning is near the stability limit, the atmosphere becomes extended, and a wind drives mass loss, as may be the case in the brightest supersoft source candidate in M81. In addition, the energy calibration of the BI devices at low photon energies is uncertain and could also have a significant effect on the results reported here.

Many of these uncertainties may be resolved or at least mitigated as pending *Chandra* observations of well-studied supersoft sources are analyzed and compared to previous observations and to specific theoretical expectations. High-resolution grating spectroscopy will be indispensible in this regard since many of the calibration uncertainties can be circumvented while, at the same time, models for the X-ray spectra can be more tightly constrained. An example of the richness of such a spectrum is that of CAL 83 obtained by the *XMM-Newton* Reflection Grating Spectrometer (Paerels et al. 2001). The population of supersoft source candidates discovered in M81 also reveals the value of isolating sources to investigate their local environments and of obtaining precise locations for future observations at X-ray and other wavelengths.

In spite of the current uncertainties, the remarkable properties deduced for the brightest supersoft source candidate in M81 should not be overlooked. This source exhibits large variations in X-ray brightness on timescales of order of hours yet maintains a high average X-ray brightness throughout the roughly 8 yr span of combined *ROSAT* and *Chandra* observations of the region. In the context of the nuclear-burning WD scenario, its high temperature and luminosity imply a high mass, near the Chandrasekhar limit for WDs, and a high accretion rate, above that for steady state nuclear burning. While optical monitoring would be difficult at best, future observations are strongly encouraged to more fully understand this source. The accurate location provided in Table 1 should aid substantially in this regard.

6.2. *Observations of Other Galaxies*

The most extensive study of supersoft sources in an external spiral galaxy similar to our own and M81 is the *ROSAT* survey of M31 (Supper et al. 1997; Kahabka 1999). Based on hardness ratios, Supper et al. (1997) identified 15 supersoft source candidates not associated with supernova remnant (SNR) or foreground objects in a 6.3 deg^2 M31 field. Kahabka (1999), using a slightly modified selection criteria, identified an additional 26 candidates in the field. Kahabka (1999) found that a total of seven of the combined 41 supersoft sources are within the $\sim$6 kpc bulge of M31, with the remainder evenly distributed over $\sim$12–25 kpc radii. The lack of detected sources in the $\sim$6–12 kpc region was explained as a consequence of a higher H column within this annulus. Kahabka (1999) suggests that the spatial distribution favors a disk population of younger stars by comparing to the populations of Cepheids and (older) blue stars. The supersoft source distribution does not follow that of novae, which follow the old stellar population of bulge stars. After accounting for possible foreground objects and SNRs, Kahabka (1999) finds one bulge source for every four to seven disk sources. This is marginally less than reported here for M81, where four bulge sources were found for an extrapolated total population of $9/0.57 \sim 16$ supersoft sources within the D_{25} area of M81. Kahabka (1999) also estimates the temperatures for all the sources and finds that they range from $\sim$30 to 60 eV, typically, up to $\sim$73 eV for the recurrent transient RX J0045.4+4154. The latter source is also one of the brightest with an inferred $L_{\rm bol} \sim 10^{38}$ ergs s^{-1} (White et al. 1995).

A more detailed comparison between the supersoft source populations of M31 and M81 must await further analysis of the extensive *Chandra* M31 data set. Only then can many of the instrumental selection effects be eliminated. In the interim, comparison to other *Chandra*-observed galaxies must suffice.

Numerous deep observations of nearby galaxies have been performed by *Chandra* in the $\sim$2 yr since its launch. Discovery (or lack thereof) of supersoft source candidates has been reported in the literature for only a few galaxies. Sarazin, Irwin, & Bregman (2000, 2001) report three supersoft sources in a sample of 90 point sources in the elliptical galaxy NGC 4697 to a limiting luminosity of $\sim 5 \times 10^{37}$ ergs s^{-1} based on hardness ratios. No supersoft sources were discovered in M84, an elliptical galaxy in the core of the Virgo Cluster, based on the hardness ratio criteria (Finoguenov & Jones 2002). Pence et al. (2001) report the discovery of 10 supersoft sources among 110 objects in M101 using color definitions different than those defined here. Pence et al. (2001) combined the spectra of the three most luminous supersoft sources, reportedly having similar spectral shapes, and find a best-fit blackbody temperature of 72 ± 2 eV and a mean (unabsorbed) luminosity of 1.4×10^{38} ergs s^{-1}. These values are similar to the brightest supersoft sources in M81 with the exception of source N1, which has an unabsorbed flux 5–8 times higher. The remaining seven supersoft sources in M101 have a distinctly softer spectrum. When combined, the best-fit blackbody temperature is 47 ± 2 eV, and unabsorbed luminosity is $L_{\rm X} = 1.1 \times 10^{37}$ ergs s^{-1} for a column fixed to the Galactic value ($N_{\rm H} = 1.2 \times 10^{20}$ cm^{-2}). Again, these values are consistent with those estimated here for the weak sources in M81, although, as shown above, a temperature of order of 40–50 eV is expected on the basis of instrumental selection effects and the shape of the parent population estimated from population synthesis models. The position of only one supersoft source candidate lies within the bulge of M101. However, M101 has a later Hubble type, Scd, and hence a smaller bulge than M81 (Sab), extending only to $\sim$0.′75, or approximately 3% of the S3 viewing field analyzed by Pence et al. (2001).

These comparisons are intriguing. They suggest that perhaps there is another supersoft source population of anomolously X-ray bright and hot objects in nearby galaxies similar to our own. Care must be exercised, of course, since there are, to date, only a handful of objects with these properties, no corroborating evidence in support of this conjecture from other wavebands, and no satisfactory theory predicting such extreme X-ray behavior. These comparisons also suggest a trend across the Hubble sequence with fewer supersoft sources in early-type galaxies compared to late types. The supersoft sources appear to be associated with the younger population of stars found on spiral arms, although some are found in the relatively old population of bulge stars. Irregular galaxies would then have a disproportionate number of supersoft sources. Di Stefano & Rappaport (1994) estimate 125 and 25 supersoft sources are active in the LMC and SMC, respectively, based on their blue luminosities relative to M31. Eight supersoft sources have been observed in the LMC and four in the SMC. This sug-

gests that either the population estimate is low or the observed fraction is high for these two galaxies. Of course, there is a strong selection bias that must be taken into account.

We thank A. Ibragimov for constructing the WD model atmospheres used in this work, A. Shafter for providing an Hα image of the field and for information on nova rates, T. Pannuti for radio data analysis, and M. McCollough for analyzing archival *HST* WFPC2 data. K. W. and V. S. thank M. Weisskopf for funding their visits to MSFC. Support for this research was provided in part by NASA *Chandra* grant GO 0-1058X to D. A. S. and by Russian Basic Research Foundation grant 99-02-17488 to V. S.

REFERENCES

Anders, E., & Grevesse, N. 1989, Geochim. Cosmochim. Acta, 53, 197
Arnaud, K. 1996, in ASP Conf. Ser. 101, Astronomical Data Analysis Software and Systems V, ed. G. Jacoby & J. Barnes (San Francisco: ASP), 17
Brown, T., Cordova, F., Ciardullo, R., Thompson, R., & Bond, H. 1994, ApJ, 422, 118
de Grijs, R., O'Connell, R. W., & Gallagher, J. S., III 2001, AJ, 121, 768
Della Valle, M., & Livio, M. 1994, A&A, 286, 786
Dere, K. P., Landi, E., Mason, H. E., Monsignori Fossi, B. C., & Young, P. R. 1997, A&AS, 125, 149
de Vaucouleurs, G., de Vaucouleurs, A., Corwin, H. G., Jr., Buta, R. J., Paturel, G., & Fouque, P. 1991, Third Reference Catalogue of Bright Galaxies (NewYork: Springer)
Devereux, N. A., Jacoby, G., & Ciardullo, R. 1995, AJ, 110, 1115
Di Stefano, R., & Nelson, L. A. 1996, in Supersoft X-Ray Sources, ed. J. Greiner (Berlin: Springer), 3
Di Stefano, R., Paerels, F., & Rappaport, S. 1995, ApJ, 450, 705
Di Stefano, R., & Rappaport, S. 1994, ApJ, 437, 733
Ebisawa, K., et al. 2001, ApJ, 550, 1007
Finoguenov, A., & Jones, C. 2002, ApJ, in press
Freedman, W. L., et al. 1994, ApJ, 427, 628
Greiner, J. 1996, in Supersoft X-Ray Sources, ed. J. Greiner (Berlin: Springer), 299
———. 2000a, NewA, 5, 137
———. 2000b, NewA Rev., 44, 149
Hachisu, I., Kato, M., & Nomoto, K. 1996, ApJ, 470, L97
Heise, J., van Teeseling, A., & Kahabka, P. 1994, A&A, 288, L45
Hill, J. K., et al. 1992, ApJ, 395, L37
Hughes, J. P. 1994, ApJ, 427, L25
Iben, I., Jr. 1982, ApJ, 259, 244
Iben, I., Jr., & Livio, M. 1993, PASP, 105, 1373
Iben, I., Jr., & Tutukov, A. V. 1985, ApJS, 58, 661
———. 1989, ApJ, 342, 430
———. 1994, ApJ, 431, 264
Immler, S., & Wang, Q. D. 2001, ApJ, 554, 202
Jacoby, G. H., Ciardullo, R., Ford, H. C., & Booth, J. 1989, ApJ, 344, 704
Jordan, S., Schmutz, W., Wolff, B., Werner, K., & Mürset, U. 1996, A&A, 312, 897
José, J., Hernanz, M., & Isern, J. 1993, A&A, 269, 291
Kaaret, P., Prestwich, A. H., Zezas, A., Murray, S. S., Kim, D.-W., Kilgard. R. E., Schlegel, E. M., & Ward, M. J. 2001, MNRAS, 321, L29
Kahabka, P. 1999, A&A, 344, 459
Kahabka, P., Hartmann, H. W., Parmar, A. N., & Negueruela, I. 1999a, A&A, 347, L43
Kahabka, P., Parmar, A. N., & Hartmann, H. W. 1999b, A&A, 346, 453
Kahabka, P., & van den Heuvel, E. P. J. 1997, ARA&A, 35, 69
Kato, M. 1997, ApJS, 113, 121
Kaufman, M., Bash, F. N., Crane, P. C., & Jacoby, G. H. 1996, AJ, 112, 1021
Kaufman, M., Bash, F. N., Hine, B., Rots, A. H., Elmegreen, D. M., & Hodge, P. W. 1989, ApJ, 345, 674
Kong, X., et al. 2000, AJ, 119, 2745
Lewin, W. H. G., Van Paradijs, J., & Taam, R. E. 1995, in X-ray Binaries, ed. W. H. G. Lewin, J. van Paradijs, & E. P. J. van den Heuvel (Cambridge: Cambridge Univ. Press), 175
Livio, M. 1992, ApJ, 393, 516
Magrini, L., Perinotto, M., Corradi, R. L. M., & Mampaso, A. 2001, A&A, 379, 90
Makishima, K., Maejima, Y., Mitsuda, K., Bradt, H. V., Remillard, R. A., Tuohy, I. R., Hoshi, R., & Nakagawa, M. 1986, ApJ, 308, 635
Makishima, K., et al. 2000, ApJ, 535, 632
Matonick, D. M., & Fesen, R. A. 1997, ApJS, 112, 49
Matsumoto, H., Tsuru, T. G., Koyama, K., Awaki, H., Canizares, C. R., Kawai, N., Matsushita, S., & Kawabe, R. 2001, ApJ, 547, L25
Mihalas, D. 1978, Stellar Atmospheres (San Francisco: Freeman)
Mitsuda, K., et al. 1984, PASJ, 36, 741
Motch, C., Hasinger, G., & Pietsch, W. 1994, A&A, 284, 827
Mukai, K. 1993, Legacy, 3, 21
Paczynski, B. 1971, Acta Astron., 21, 417
Paerels, F., Rasmussen, A. P., Hartmann, H. W., Heise, J., Brinkman, A. C., de Vries, C. P., & den Herder, J. W. 2001, A&A, 365, L308
Parmar, A. N., Kahabka, P., Hartmann, H. W., Heise, J., Martin, D. D. E., Bavdaz, M., & Mineo, T. 1997, A&A, 323, L33
Parmar, A. N., Kahabka, P., Hartmann, H. W., Heise, J., & Taylor, B. G. 1998, A&A, 332, 199
Pence, W. D., Snowden, S. L., Mukai, K., & Kuntz, K. D. 2001, ApJ, 561, 189
Rappaport, S., Chiang, E., Kallman, T., & Malina, R. 1994a, ApJ, 431, 237
Rappaport, S., Di Stefano, R., & Smith, J. D. 1994b, ApJ, 426, 692
Reichen, M., Kaufman, M., Blecha, A., Golay, M., & Huguenin, D. 1994, A&AS, 106, 523
Remillard, R. A., Rappaport, S., & Macri, L. M. 1995, ApJ, 439, 646
Sarazin, C. L., Irwin, J. A., & Bregman, J. N. 2000, ApJ, 544, L101
———. 2001, ApJ, 556, 533
Schaeidt, S., Hasinger, G., & Trümper, J. 1993, A&A, 270, L9
Shakura, N. I., & Sunyaev, R. A. 1973, A&A, 24, 337
Sion, E. M., & Starrfield, S. G. 1994, ApJ, 421, 261
Southwell, K. A., Livio, M., Charles, P. A., O'Donoghue, D., & Sutherland, W. J. 1996, ApJ, 470, 1065
Supper, R., Hasinger, G., Pietsch, W., Trümper, J., Jain, A., Magnier, E. A., Lewin, W. H. G., & van Paradijs, J. 1997, A&A, 317, 328
Tennant, A. F., Wu, K., Ghosh, K. K., Kolodziejczak, J. J., & Swartz, D. A. 2001, ApJ, 549, L43
Thomasson, M., & Donner, K. J. 1993, A&A, 272, 153
Townsley, L. K., Broos, P. S., Garmire, G. P., & Nousek, J. A. 2000, ApJ, 534, L139
van den Heuvel, E. P. J., Bhattacharya, D., Nomoto, K., & Rappaport, S. A. 1992, A&A, 262, 97
Verbunt, F., & van den Heuvel, E. P. J. 1995, in X-Ray Binaries, ed. W. H. G. Lewin, J. van Paradijs, & E. P. J.van den Heuvel (Cambridge: Cambridge Univ. Press), 457
Verner, D. A., & Yakovlev, D. G. 1995, A&AS, 109, 125
Verner, D. A., Yakovlev, D. G., Band, I. M., & Trzhaskovskaya, M. B. 1993, At. Data Nucl. Data Tables, 55, 233
Wang, Q. 1991, MNRAS, 252, P47
White, N. E., Giommi, P., Heise, J., Angelini, L., & Fantasia, S. 1995, ApJ, 445, L125
Yungelson, L., Livio, M., Truran, J. W., Tutukov, A., & Fedorova, A. 1996, ApJ, 466, 890